PFC/JA-81-5

CONTINUUM X-RAY EMISSION
FROM THE ALCATOR A TOKAMAK

John E. Rice
Kim Molvig
Heikki I. Helava

April, 1981

CONTINUUM X-RAY EMISSION FROM THE ALCATOR A TOKAMAK

John E. Rice and Kim Molvig

Plasma Fusion Center and Francis Bitter National Magnet Laboratory
Massachusetts Institute of Technology
Cambridge, Massachusetts 02139

and

Heikki I. Helava

Physics International Company
San Leandro, California 94577

Abstract

X-rays from 1 to 25 keV emitted by the Alcator A device have been collected with a Si(Li) detector and pulse height analysis system. Under normal operating conditions, spectra are thermal indicating clean ($Z_{eff} \sim 1$), Maxwellian distributions. Temperature profiles are provided. When $v_d/v_{th} \gtrsim .03$, the X-ray spectra become non-thermal, reflective of non-Maxwellian distributions. The observed non-thermal behaviour increases with minor radius and poloidal symmetry, is correlated with poor energy confinement and cannot be accounted for by classical electric field driven perturbation theory. Radial electron diffusion is discussed.

I. Introduction.

This purpose of this article is to account for the X-radiation spectra from 1 to 25 keV emitted by the Alcator tokamak[1] under various conditions. Similar studies have been performed on other tokamaks such as ST[2], Pulsator[3], TFR[4], and T-10[5]. The observed spectra involve both continuous and line radiation and the overall understanding requires both a knowledge of the electron distribution function and the impurity species. The primary continuum radiation process is bremsstrahlung -- X-rays emitted in collisions between electrons and ions. The shape of the spectrum reveals the details of the $v > v_{th}$ region of the electron distribution function. To this end, knowledge of the bremsstrahlung cross section is required. In section II, a general expression for the bremsstrahlung cross section is provided; the result of numerical determination of the dipole radiation matrix elements. Calculation of the bremsstrahlung spectrum from an arbitrary distribufunction is then outlined. In section III, the secondary continuum process, radiative recombination, is discussed and estimates of the contribution to the bremsstrahlung spectrum are given. In section IV, the classical electric field driven distribution functions are reviewed, including the effects of magnetic trapping and magnetic field ripple, in order to model the expected distribution in a tokamak.

Section V is devoted to the study of thermal X-ray spectra. Temperature profiles are provided. The observed changes of the central electron temperature and overall profile shape with varying current, toroidal field and loop voltage, are explained in terms of a model which assumes classical resistivity to be valid and that the central safety factor, $q_o \leq 1$.

The concern of section VI is non-thermal X-ray spectra. Observations of non-thermal spectra on other machines[2,3,5] have been made but no quantitative discussions have been presented. Such spectra observed on Alcator are unable to be accounted for by classical electric field driven perturbation theory. The effects of fast electrons trapped in the toroidal field ripple cannot explain the observed non-thermal distributions either. Spatial dependence of the non-thermal behaviour is documented as well as the scalings with plasma density and current. Energy confinement times are calculated and the association of non-thermal distributions and poor energy confinement is indicated.

The connection between non-thermal distributions and poor energy confinement is formalized in section VII via the inclusion of a spatial diffusion term in the electron kinetic equation. From this the heat transport equation is obtained and the perturbative solution to the kinetic equation is presented. The link between the non-thermal portion of the distribution and the outward electron heat flux is the diffusion coefficient.

In section VIII, the diffusion coefficient is obtained from the non-thermal X-ray spectra and the global power balance equation is satisfied, justifying the kinetic equation of section VII. Scalings of the diffusion coefficient are provided.

In section IX, the kinetic diffusion equation of section VII is derived by including the effect of a small, random radial magnetic field in the drift kinetic equation. The magnetic field fluctuation level is determined from the observed diffusion coefficient of section VIII. The hypothesis that magnetic fluctuations are the source of anomalous heat loss in Alcator is offered.

Note that all X-ray spectra presented here are averaged over sawtooth oscillations.

Scientific notation employed here will, for example, write $3.2\ \enclose{circle}{-8}$ instead of $3.2\mathrm{x}10^{-8}$ in order to emphasize the exponent, assuming base 10 to be understood.

II. Bremsstrahlung

Bremsstrahlung is the process in which electrons undergo radiative transitions between positive energy states in a Coulomb field. Since there exists a continuum of energy levels, the photons emitted comprise a continuous spectrum. The non-relativistic problem was first addressed by Sommerfeld[6] who obtained initial and final state wave functions for the positive energy states, and the corresponding electric dipole moments for an unscreened Coulomb potential. Since expressions for the dipole radiation matrix elements of the individual polarizations of the emitted photons do not exist in closed form, numerical integrations are required to obtain the bremsstrahlung cross section. The cross section, or probability per unit time that an electron of energy ε_o will emit a photon of energy $h\nu$ into the solid angle $d\Omega$, is

$$\sigma(\varepsilon_o,h\nu)\,d\nu\,d\Omega = I_\nu^{(\theta)}\,\frac{d\nu\,d\Omega}{h\nu} \qquad \text{cm}^2 \qquad (1)$$

where $I_\nu^{(\theta)}$ is a function of the dipole matrix elements and may be computed using a method outlined by Weinstock[7]. This cross section, integrated over angles of the outgoing photon, has been expressed in closed form by Sommerfeld and Maue[8]:

$$\sigma(\varepsilon_o,h\nu)\,d\nu = \frac{8\pi}{3}\,\frac{e^2h}{m^2c^3}\,\frac{dh\nu}{h\nu}\,\frac{\eta_o^2\,x}{(e^{2\pi\eta_o}-1)(1-e^{-2\pi\eta_f})}\,\frac{d|F|^2}{dx} \qquad \text{cm}^2 \qquad (2)$$

where $\eta_{o,f} \equiv Z\sqrt{\dfrac{13.59\text{eV}}{\varepsilon_{o,f}}}$ is a quantum number for the given state (the subscript $_o$ denotes initial, $_f$ denotes final), related to the photon energy by the Rydberg formula $h\nu = Z^2\ 13.59\text{eV}\left[\dfrac{1}{\eta_o^2} - \dfrac{1}{\eta_f^2}\right]$, $x \equiv \dfrac{4\eta_o\eta_f}{(\eta_f^2-\eta_o^2)}$

and F is the ordinary hypergeometric function $F = {}_2F_1(j\eta_o, j\eta_f; 1; -x)$. This integrated cross section is appropriate for calculating the energy spectrum of X-rays, $I(h\nu)$, from an isotropic incoming electron distribution function, $f(\varepsilon_o)$, via the convolution

$$I(h\nu) = \sum_i n_i Z_i^2 \int_{h\nu}^{\infty} \sqrt{\frac{2\varepsilon_o}{m}}\, \nu\sigma(\varepsilon_o, h\nu) f(\varepsilon_o)\, d\varepsilon_o \quad \frac{\text{energy}}{\text{unit energy-sec-cm}^3} \tag{3}$$

where n_i is the number density of stationary ions of charge Z_i (creating the Coulomb field) in cm^{-3} and $f(\varepsilon_o)$ is normalized such that $\int f(\varepsilon_o)\, d\varepsilon_o = n_e\ \text{cm}^{-3}$, the number density of electrons. For a Maxwellian electron distribution function of temperature T_e, this integral is equal to[9]

$$I(h\nu) = 2.60 \enclose{circle}{-14}\, n_e \sum_i n_i Z_i^2 \sqrt{\frac{13.59\text{eV}}{T_e}}\; e^{-h\nu/T_e}\, \bar{g} \quad \frac{\text{energy}}{\text{unit energy-sec-cm}^3} \tag{4}$$

where $\bar{g}$ is an average Gaunt factor, plotted in Fig. 1[10] for different values of T_e. Also shown is a reasonable approximation to $\bar{g}$, $\sqrt[3]{\frac{T_e}{h\nu}}$, which will be used in all subsequent calculations involving Maxwellian distributions.

For non-isotropic distribution functions, the expressions for the radiation intensities of the individual polarizations must be used in Eq. 1,

$$\sigma(\varepsilon_o, h\nu)\, d\nu\, d\Omega = \frac{1}{h\nu}\left\{ I_x(\varepsilon_o, h\nu) \sin^2 \textcircled{H} + I_y(\varepsilon_o, h\nu) + I_z(\varepsilon_o, h\nu) \cos^2 \textcircled{H} \right\} d\nu\, d\Omega \quad \text{cm}^2 \tag{5}$$

where the electron is incident along the x-axis as shown in Fig. 2. If the electron spin is neglected, $I_y = I_z$. I_x and I_y have been tabulated for $\varepsilon_o < 1$ keV by Kirkpatrick and Wiedmann[11] and approximate algebraic formulae are given. These tables have been extended to $\varepsilon_o \leq 13.59$ keV, and some results for I_y are shown in Fig. 3 along with the approximation $I_y'' / h \equiv \frac{6.06 \textcircled{-26}}{\varepsilon_o} \left[\frac{1}{\frac{h\nu}{\varepsilon_o} + .255} - .813 \right] \frac{\mathrm{cm}^2}{\mathrm{ster}}$ where h is Planck's constant, and ε_o is in keV. This approximation is accurate to greater than 10% over most of the regions of interest, as is $I_x'' / h \equiv \frac{1.18 \textcircled{-25}}{\varepsilon_o} \frac{\mathrm{cm}^2}{\mathrm{ster}}$ for I_x.

The X-ray spectrum from a non-isotropic electron distribution function, $f(\bar{v})$, may then be calculated,

$$I(h\nu) = \sum_i n_i Z_i^2 \int_{\sqrt{\frac{2h\nu}{m}}}^{\infty} \int_{4\pi} \frac{v}{h} \left\{ I_x \sin^2 \textcircled{H} + I_y (1+\cos^2 \textcircled{H}) \right\} f(\bar{v})\, d\Omega\, v^2 dv \qquad (6)$$

where $\int v^2 \, dv \, d\Omega \, f(\bar{v}) = n_e \ \mathrm{cm}^{-3}$.

In order to test the quality of approximations to $I_x(\varepsilon_o, h\nu)$ and $I_y(\varepsilon_o, h\nu)$, I_x'' and I_y'' have been inserted into Eq. 6, for a Maxwellian distribution function, to compare with Eq. 4. The result is shown in Fig 4. The agreement is quite good, justifying future use of I_x'' and I_y''.

III. Radiative Recombination

Radiative recombination is the process by which electrons undergo transitions from initial positive energy states in a Coulomb field to final bound states. The spectrum of emitted photons is then continuous but has finite jumps at energies corresponding to the ionization potentials of the final bound levels. The determination of the cross section for this process from the dipole matrix elements is similar to the bremsstrahlung calculation except that the final state involves bound level wave functions. For high Z materials these wave functions are not well known. The problem was first discussed in detail by Menzel and Pekeris[12] and extended by Karzas and Latter[10] and by Brussaard and van de Hulst[13] who considered the case of the emitted spectrum from a Maxwellian electron distribution. The essential result is that $\bar{g}$ in Eq. 4 be replaced by $\bar{g} + f_i(T,h\nu)$. For an initially completely stripped ion, (neglecting any difference between subshells)

$$f_i(T,h\nu) = 2\theta_i \sum_{n=m_i(h\nu)}^{\infty} \frac{e^{\theta_i/n^2}}{n^3} g_n(h\nu) \tag{7}$$

where $\theta_i = Z_i^2$ (13.59 eV/T), n is the principle quantum number of the final hydrogenlike state, $m_i(h\nu)$ is equal to the n for the lowest bound level to which emission at energy $h\nu$ can occur, $[m_i(h\nu) - 1 < h\nu/13.59\ Z_i^2\ \mathrm{eV} < m_i(h\nu)]$ and $g_n(h\nu)$ is a function which has been tabulated in ref. 10. To illustrate the contribution of recombination to the hydrogenic bremsstrahlung spectrum under "dirty" Alcator conditions, the enhanced spectrum has been calculated for the case of a .17% oxygen contamination[14] in an 870 eV plasma (Z_{eff} = 1.1). The result is shown in Fig. 5. The effect of the oxygen is to produce a discontinuity at 870 eV (the ionization potential of the K shell in oxygen) and to enhance the spectrum in intensity above that point by about a factor of 2. This enhancement can provide a sensitive measurement of Z_{eff} provided the ion species are properly identified[2]. The assumption that the oxygen is initially stripped is a good one since this condition is realized for an electron temperature > 220 eV[15] which is the case for most of the volume of plasma in Alcator.

Calculation of the recombination spectrum from transitions to the L shell in molybdenum is considerably more difficult because many-electron wave functions are not well known. This problem has been discussed by Equipe TFR[4]. At the temperatures of interest (∿ 1 keV), the fraction of neonlike molybdenum is very small, so one would expect recombination to the L shell to be unimportant. An estimate of the relative importance to proton bremsstrahlung may be obtained by inserting Eq. 7 into Eq. 4, and taking the ratio,

$$\frac{I_{Mo}(h\nu)}{I_{brem}(h\nu)} \approx \frac{n_{mo} Z_{mo}^2}{n_e \bar{g}} \left\{ \bar{g} + \frac{2\theta_i}{n^2} \frac{e^{\theta_i/n^2}}{n} g_n(h\nu) \right\} F_i \qquad (8)$$

where F_i is the ratio of Mo^{33+} to the predominant charge state at a given temperature. At T_e = 870 eV, the predominant charge state is[16] Mo^{23+}, F_i is .003 (found by taking the ratio of ionization coefficients at 870 eV[15]), and $\theta_i/n^2 = 4.6$ (n = 2 and the ionization potential out of the L shell in molybdenum is[17] ∿ 4 keV). Taking $n_{Mo} = 3\,(10)\,\text{cm}^{-3}$, $n_e = 6\,(14)\,\text{cm}^{-3}$, $Z_{Mo} \simeq 33$, and setting $\bar{g} = g_n(h\nu) = 1$, Eq. 8 yields .08. On the basis of this calculation, one would expect to see an 8% jump in the continuum spectrum at hν $\sim$ 4keV. Recombination into the L shell of molybdenum is then probably not important in Alcator X-ray spectra.

IV. The Electron Distribution Function

The equilibrium electron distribution function in the absence of externally applied forces (but with a mechanism for confinement and energy replenishment) is the Maxwellian distribution,

$$f_m = \frac{n}{\pi^{3/2} v_{th}^3} e^{-v^2/v_{th}^2} \tag{9}$$

where $mv_{th}^2/2$ is the electron temperature. Since it is symmetric about $v = 0$, the Maxwellian distribution cannot carry current. This function may be altered to accomodate current:

$$f = \frac{n}{\pi^{3/2} v_{th}^3} e^{-v_\perp^2/v_{th}^2} e^{-(v_\parallel - u_o)^2/v_{th}^2} \tag{10}$$

where u_o is the drift velocity and $\langle v_\parallel \rangle = \int \frac{f v_\parallel d^3v}{n} = v_{th} e^{-\zeta^2} \left\{\zeta + \zeta^3 + \ldots\right\}$ $\approx u_o$ for small u_o with $\zeta \equiv u_o/v_{th}$. For a 1 keV plasma, $v_{th}/c = .063$, for $n = 4$ ⑭ cm^{-3} and $I = 150$ kA (central current density $j_\parallel =$ $2.9 \mathrm{kAcm}^{-2}$), $\langle v_\parallel \rangle = j_\parallel/ne = .0015\ c$ and $\zeta = .024$. Thus, only a small drift is required to carry the current in such a case.

The proper approach to determine the distribution function is to calculate the response to an external electric field, a situation which has been considered in detail by Cohen, Spitzer and Routly[18] and improved upon by Spitzer and Härm[19]. The problem is formulated as the search for a steady state solution to the Boltzmann equation which ignores close encounters but includes distant electron-electron collisions. The equation becomes the Fokker-Planck equation which can be solved numerically under the assumption that

$$f_{s-H} = f_m(1+D(v/v_{th})\cos\theta) \tag{11}$$

where $D << 1$, and θ is the angle between E and v. To a good approximation,

$$D(v/v_{th}) = \frac{E}{E_r}\left\{-.086+1.48(v/v_{th})^2+.105(v/v_{th})^4\right\} \tag{12}$$

where $E_r \equiv -\pi ne^3 \ln(\Lambda)/T$. Eq. 11 is inappropriate when $E_r/E \sim (v/v_{th})^4$. For the sake of comparison, Eqs. 9 and 11 with $E/E_r = .05$ are shown in Fig. 6. An expression for the electrical conductivity may be found from Eq. 11 by taking the moment

$$\sigma \equiv \frac{e}{E}\int v\cos\theta f_{s-H} v^2 dv \sin\theta d\theta d\phi = \frac{1.74\ \boxed{14}\ T_e^{3/2}}{(Z_{eff} \ln\Lambda)}\ \sec^{-1} = \frac{194 T_e^{3/2}}{(Z_{eff})\ln\Lambda}(\text{ohm-cm})^{-1} \tag{13}$$

with T_e in eV.

Kruskal and Bernstein[20] have addressed the subject of the distribution in an electric field for $v/v_{th} > (E_r/E)^{1/4}$ by considering the high velocity expansion of the Fokker-Planck equation,

$$xg_x = (1-\mu^2)g_{\mu\mu} - 2\mu g_\mu + x^4\mu g \tag{14}$$

where $f = f_m g$, $x \equiv v/v_{th}(E/E_r)^{1/4}$, $\mu \equiv \cos\theta$ and the subscripts denote partial derivatives. An exact solution to this equation is

$$g = \sum_{n=0}^{\infty}\sum_{\ell=0}^{n} g_\ell^n P_\ell(\mu)\ x^{4n} \tag{15}$$

where the $P_\ell(\mu)$s are Legendre polynomials and the g_ℓ^ns satisfy the recursion formula

$$g_{\ell}^{n} = \frac{1}{4n+\ell(\ell+1)}\left[\frac{\ell}{2\ell-1}\, g_{\ell-1}^{n-1} + \frac{\ell+1}{2\ell+3}\, g_{\ell+1}^{n-1}\right] \qquad (16)$$

subject to the conditions $g_0^0 = 1$, $g_{\ell>0}^0 = g_{n+1}^{n-1} = g_n^{n-1} = 0$. So to second order in E/E_r,

$$f = f_m\left(1+\frac{1}{6}\cos\theta\frac{E}{E_r}\left(\frac{v}{v_{th}}\right)^4 + \left(\frac{1}{336} + \frac{1}{84}\cos^2\theta\right)\left(\frac{E}{E_r}\right)^2\left(\frac{v}{v_{th}}\right)^8 + \ldots\right) \qquad (17)$$

valid until $v/v_{th} \sim (2E_r/E)^{1/2}$. $f/f_m - 1$ for Eqs. 11 and 17 is plotted in Fig. 7 for $E/E_r = .05$ and $\cos\theta = 1$.

No distribution function in an axisymmetric toroidal confinement device would be complete without inclusion of the effects of magnetic trapping. The problem was originally discussed in detail by Rosenbluth, Hazeltine, and Hinton[21], who accounted for the toroidal geometry by assuming a magnetic field structure $(B_r, B_\theta, B_\phi) = (0, b(r)/h, B_o/h)$ with $b(r) \ll B_o$ and $h \equiv 1 + r/R\cos\theta$, $r/R \ll 1$ and where the geometry is shown in Fig. 8. The distribution function was determined by using a variational principle, subject to the condition that the trapped electron collision frequency is much less than the bounce (in the banana orbit) frequency, $R/r\ \nu_c \ll \omega_b$ where $\nu_{eff} \equiv R/r\nu_c = 8\pi e^4 n \ln(\Lambda) R/rm^2v^3$ and $\omega_b \cong \sqrt{\frac{r}{R}}\,\frac{vb(r)}{rB_o}$. This condition may be written

$$\frac{1}{\nu_*}\left(\frac{v}{v_{th}}\right)^4 \equiv \frac{\omega_b}{\nu_{eff}} = \left(\frac{r}{R}\right)^{3/2} \textcircled{10}\, \frac{T_o^2}{n(r)q(r)}\left(\frac{v}{v_{tho}}\right)^4 \gg 1 \qquad (18)$$

where T_o is in eV, $n(r)$ in cm^{-3}, $\ln\Lambda \sim 14$, $R = 54cm$ and $q(r)$ is the safety factor, $rB_o/Rb(r)$. This condition for being in the banana regime is not satisfied for thermal electrons at moderate radii during most Alcator operation. However, under conditions of low density and high current, electrons of interest for x-rays ($v > v_{th}$) should be trapped, according to Eq. 18, at the larger radii. Trapping is especially important for the current carrying electrons. From Eq. 12 it can be shown that the average velocity of the current carrying electrons,

$$v_c \equiv \int vD\left(\frac{v}{v_{th}}\right)d^3v \Big/ \int D\left(\frac{v}{v_{th}}\right)d^3v \tag{19}$$

is $\simeq 1.7\, v_{th}$. So, for the current carriers, the inequality Eq. 18 may be satisfied for values of the collisionality parameter ν_* as large as 9. This point has been emphasized by Coppi[22].

The result for the distribution function, neglecting terms of order ρ/L where ρ is the gyroradius and L is a gradient scale length, is

$$f = f_m[1+\hat{f}] \equiv f_m\left[1 - H\,(\lambda_c-\lambda)D\left(\frac{v}{v_{th}}\right)\frac{v}{2}\int_{\lambda_c}^{\lambda}\frac{d\lambda}{\left(\frac{1}{2\pi}\int_0^{2\pi}d\theta v_{\parallel}\right)}\right] \tag{20}$$

where H is the step function, $\lambda \equiv \frac{v_\perp^2}{v^2}\left(1+\frac{r}{R}\cos\theta\right)$ and $\lambda_c \equiv 1-\frac{r}{R}$. This is simply a modification of the Spitzer-Härm result to include the effects of trapped electrons, and is equal to Eq. 11 for $r/R = 0$. If it is assumed that $v_\parallel$ is independent of θ, then Eq. 20 becomes

$$\hat{f} = H\left[\frac{v_\parallel^2}{v^2} - \frac{r}{R}\left(1+\frac{v_\perp^2}{v^2}\cos\theta\right)\right]D\left(\frac{v}{v_{th}}\right)h\left[\frac{v_\parallel}{|v|} - \frac{v_\parallel}{|v_\parallel|}\sqrt{1-\frac{\lambda_c}{h}}\right]. \tag{21}$$

To estimate the magnitude of the effect on the Spitzer-Härm distribution, consider Eq. 21 with $v_{\parallel} = v$, $r/R = .07$ ($r = 3.8\text{cm}$ in Alcator), and $\theta = 0^{\circ}$ and 180°,

$$\hat{f} = \begin{cases} .68D\left(\frac{v}{v_{th}}\right) & \theta = 0^{\circ} \\ .93D\left(\frac{v}{v_{th}}\right) & \theta = 180^{\circ} \ . \end{cases} \qquad (22)$$

The essential result is that the Spitzer-Härm distribution is multiplied by the fraction of circulating electrons. For a given driving field, only the untrapped electrons can respond, and on the outside ($\theta \cong 0^{\circ}$) of the machine, the perturbation to the Maxwellian is reduced. It can only equal the Spitzer-Härm distribution at the largest. This effect manifests itself in alterations of the conductivity, which from Eqs. 21 and 13 becomes,

$$\sigma_b = 1.7 \textcircled{14} \frac{T_e^{3/2}}{\ln\Lambda} \left[1 - 1.95 \sqrt{\frac{r}{R}}\right] \text{sec}^{-1} \qquad (23)$$

which is the same as Eq. 13 modified by the term in brackets.

In summary, the electric field driven electron distribution function, including the effects of magnetic trapping, has been reproduced in order to compare with observed x-ray spectra (section VI).

V. Thermal Spectra and Profiles

The x-ray spectrum from a Maxwellian electron distribution colliding with stationary ions of charge Z_i and number density n_i, including recombination radiation, is given by

$$I(h\nu) = 2.60 \enclose{circle}{-14} n_e \sum_i n_i Z_i^2 (\bar{g}_i + f_i) \sqrt{\frac{13.59\text{eV}}{T_e}}\, e^{-h\nu/T_e} \frac{\text{energy}}{\text{unit energy-cm}^3\text{-sec}} \tag{24}$$

which may be rewritten (following von Goeler[2]),

$$I(h\nu) = 2.60 \enclose{circle}{-14} n_e^2 \,\bar{g} \sqrt{\frac{13.59\text{eV}}{T_e}}\, e^{-h\nu/T_e}\, \zeta \tag{25}$$

where $\zeta (\equiv \sum_i \frac{n_i Z_i^2}{n_e} \frac{\bar{g}_i + f_i}{\bar{g}})$ is a measure of the contribution to the spectrum from impurities. Note that $f_i \ll \bar{g}$ for a high temperature hydrogen plasma. $\zeta = 1$ for a hydrogen plasma.

What is actually observed at the detector is

$$F(h\nu) \equiv \frac{\Delta N}{\Delta t \Delta V \Delta \Omega \Delta h\nu} = 2.41 \enclose{circle}{-16} \frac{\bar{g} n_e^2}{\sqrt{T_e}}\, \zeta \,\frac{e^{-h\nu/T_e}}{h\nu} \;\frac{\#\text{ photons}}{\text{sec-cm}^3\text{-solid angle-unit energy}} \tag{26}$$

(T_e is in keV and n_e is in cm^{-3}) and is related to $I(h\nu)$ by

$$I(h\nu) = h\nu \int F(h\nu)\, d\Omega \;. \tag{27}$$

The geometry of the detection system for most of the measurements presented here is shown in Fig. 9. Spatial resolution inside the plasma is about 1/2 cm and the detector is able to scan from 6 cm above to 9 cm below the center in the vacuum system with two obstructions due to limited port access. Since photons originate along a given chord, Eq. 26 must be modified to include profile effects,

$$\frac{h\nu\Delta N}{\Delta t\Delta A\Delta\Omega\Delta h\nu} = 2.41 \enclose{circle}{-16} \int_L d\ell \, \frac{n_e^2(\ell)}{\sqrt{T_e(\ell)}} \, \bar{g}(\ell)\,\zeta(\ell)\,e^{-h\nu/T_e(\ell)} \quad \frac{\text{photons}}{\text{cm}^2\text{-sec-ster}} \qquad (28)$$

where L is the chord length in the plasma, $\Delta V = \Delta A \, d\ell$, and $\Delta h\nu$ is the channel width in the multi-channel analyser (MCA). Here the variable ℓ is related to the toroidal variable r by $\ell^2 = r^2 - d^2$ where d is the distance of the viewing chord from the center of the plasma. Fig. 10 shows computed spectra (from Eq. 28) for a clean ($\zeta(\ell) = 1$) discharge with a parabolic density profile,

$$n_e(\ell) = n_o\left(1-\frac{r^2}{a_L^2}\right) = n_o\left(1-\frac{d^2}{a_L^2}-\frac{\ell^2}{a_L^2}\right) \qquad (29\text{-a})$$

(where a_L is the limiter radius (10cm), n_o is the central density) and 3 Gaussian temperature profiles,

$$T_e(\ell) = T_o e^{-r^2/a^2} = T_o e^{-d^2/a^2} e^{-\ell^2/a^2} \qquad (29\text{-b})$$

(where T_o is the central temperature) with a = 3,5,7 cm and d = 2 cm. By observing photons with energies a few times the temperature, the hottest point along the chord is predominant.

An example of a thermal spectrum is shown in Fig. 11 which was taken during the steady state portion of a 60 kG, 140 kA discharge with a line averaged density of $4.0 \enclose{circle}{14}\,\text{cm}^{-3}$. The feature at ∿ 2.7 keV is due to L line radiation from the molybdenum introduced into the plasma by interaction with the limiter and to K radiation from chlorine. A detailed discussion of this feature may be found elsewhere[23]. The curve is the expected spectrum from an 850 eV plasma with a Gaussian temperature profile with a width of 5cm as viewed along the central chord, obtained by fitting the points between 1.3 and 2.1 keV. By measuring spectra along different chords, a self consistent temperature profile may be determined. Consider for the sake of argument a Gaussian profile. For a given density and enhancement profile, a value for the width, a, is chosen and T_o is ascertained from Eqs. 28 and 29 for different values of d. a is then adjusted until all the T_o's agree. Fig. 12 shows the result of the application of this procedure to the discharge previously described. The indication is that although the profile may be slightly flatter on top than a Gaussian, this particular function is adequate (within the experimental errors). Fig. 13 shows a profile obtained for a 60 kG, 220 kA discharge with an average density of 3.7⑭ cm^{-3}. The central temperature is higher and the profile broader than in the previously described shot, and seems to be flatter than a Gaussian in the center. Shown for comparison are data from Thomson scattering and electron cyclotron emission[24] (which has been normalized to the x-ray data). Considering that the x-ray points are from a vertical scan and the other data are from horizontal scans at different toroidal locations, the agreement is quite good. The shaded regions represent the shadows of the struts in the access port and are not symmetric about the center because the detector beam line is slanted at ∿ 5° above the horizontal plane through the center of the torus.

In order to explain the changes in T_o and profile shape with variations of machine parameters such as the toroidal field, B_T, loop voltage, V_l, plasma current, I, and Z_{eff} ($\equiv \sum_i n_i Z_i^2/\sum_i n_i Z_i$), consider the following model[25]. The underlying assumptions are that the resistivity, η, (σ^{-1}) is given by Eq. 13, the temperature profile may be described by a Gaussian $T_o \exp -r^2/a^2$, and the central safety factor, q_o, is ≤ 1 (as implied by sawtooth oscillations). The plasma current is then,

$$I \equiv \int_0^{a_L} j(r)2\pi r dr = 2\pi\int_0^{a_L} \sigma(r)E(r)rdr \approx \frac{2\pi E(.194)}{Z_{eff}\ln\Lambda}\int_0^{a_L} T_e(r)^{3/2}rdr =$$

$$\frac{.194V_lT_o^{3/2}}{Z_{eff}\ln\Lambda R}\int_0^{a_L} e^{-\frac{3r^2}{2a^2}}rdr \approx \frac{.194V_lT_o^{3/2}a^2}{Z_{eff}\ln\Lambda 3R}\ (\text{kA}) \tag{30}$$

where T_o is in eV, V_l (in volts) = $2\pi RE$, R is the major radius of the torus (54cm), E is the toroidal electric field, and a is in cm. Radial variations of E, Z_{eff}, and $\ln\Lambda$ have been neglected, and $\exp -3a_L^2/2a^2 << 1$ has been assumed since, typically, $a \leq 6.5$ cm. The central safety factor may be written

$$q_o = \frac{5B_T}{\pi Rj_o} = \frac{5B_TZ_{eff}\ln\Lambda 2\pi R}{\pi R.194T_o^{3/2}V_l} = \frac{51.5B_TZ_{eff}\ln\Lambda}{T_o^{3/2}V_l} \tag{31}$$

with B_T in kG. Eq. 31 may be rewritten as follows:

$$T_o = \left[\frac{51.5B_TZ_{eff}\ln\Lambda}{V_lq_o}\right]^{2/3} \approx 84\text{eV}\left(\frac{B_T}{V_l}\right)^{2/3}\left(\frac{Z_{eff}}{q_o}\right)^{2/3} \tag{32}$$

where $\ln\Lambda \sim 14$. From Eqs. 30 and 31 there follows

$$a = 3.8\sqrt{\frac{I}{B_T}}\ \text{cm} \tag{33}$$

where q_o is assumed to be 0.9. Fig. 14 is a plot of the central temperature T_o from several thermal discharges, as a function of B_T/V_1 with Z_{eff} taken to be 1.0 (except for the helium point) and $q_o = .9$. The good agreement with the curve (Eq. 32) may be regarded as supportive of the assumption that $q_o = .9$. The actual range of B_T in Fig. 14 is from 35 to 75 kG. Fig. 15 is a plot of the Gaussian profile width, a, from several thermal discharges as a function of I/B_T. The curve is Eq. 33. The agreement is good for $a \leq 6$cm after which the assumption of a Gaussian profile is expected to fail. For example, a temperature at the limiter of 130 eV would be required for a shot with $T_o = 1$ keV and $a = 7$cm. The conclusion here is that a Gaussian profile becomes inappropriate when q at the limiter is ≤ 3, or alternatively that in such cases q_o falls below .9.

The above analysis neglects any effects of density on the temperature and profile shape. Presumably variations in density would affect the assumptions that $q_o = .9$ and that the resistivity is classical. It is known on Alcator that as the density increases, the density profile becomes more peaked[26]. Specifically, as the line averaged density changes from 2⑭ cm^{-3} to 5⑭ cm^{-3} the profile shape changes from a parabola to a $(\text{parabola})^2$. If it is assumed that $(d\ln T/dr)^{-1} \equiv a_T < (d\ln n/dr)^{-1} \equiv a_n$, then as the density is increased, one would expect the temperature profile to become narrower. Fig. 16 is a plot of the temperature profile width a vs. $I/n_o\sqrt{T_o}$. It is seen that as the density increases, a decreases, in support of the assumption that $a_T < a_n$. The curve is an empirical fit to the data.

In conclusion, for thermal discharges in Alcator, temperature profiles are adequately described by Gaussians, $Z_{eff} \sim 1$, $q_o \sim .9$, classical resistivity prevails and the temperature profile adjusts to stay narrower than the density profile in the central portion of the discharge.

VI. Nonthermal Spectra and Energy Confinement

The previous section discussed information concerning thermal spectra derived from the study of x-ray spectra. Non-thermal distributions may be examined from their subsequent x-ray spectra via Eq. 6. Most non-isotropic distribution functions are written in terms of θ $(\cos^{-1}\mu)$, the angle between the electron velocity vector and the external toroidal (electric or magnetic) field. To compute the spectrum, a coordinate transformation must first be applied to Eq. 5,

$$I_x \sin^2 \textcircled{H} + I_y (1+\cos^2 \textcircled{H}) \Rightarrow I_x (1-\sin^2\theta\sin^2\phi) + I_y (1+\sin^2\theta\sin^2\phi). \tag{34}$$

If the distribution is axisymmetric $(\partial/\partial\phi = 0)$, the ϕ integration in Eq. 6 may be performed,

$$\int_0^{2\pi} d\phi \left\{ I_x (1-\sin^2\theta\sin^2\phi) + I_y (1+\sin^2\theta\sin^2\phi) \right\} = 2\pi \left\{ I_x (1-\tfrac{1}{2}\sin^2\theta) + I_y (1+\tfrac{1}{2}\sin^2\theta) \right\} \tag{35}$$

which may be written in terms of Legendre polynomials,

$$= 2\pi \left\{ I_x (\tfrac{2}{3}P_o + \tfrac{1}{3}P_2) + I_y (\tfrac{4}{3}P_o - \tfrac{1}{3}P_2) \right\}. \tag{36}$$

Consider the x-ray spectrum from the Spitzer-Härm distribution function, found by inserting Eqs. 36 and 11 into Eq. 6,

$$I(h\nu) = \frac{2\pi n_e}{h} \int_{\sqrt{\frac{2h\nu}{m}}}^{\infty} v^3 dv f_m \int_0^{\pi} \left\{ I_x\left(\tfrac{2}{3}P_o + \tfrac{1}{3}P_2\right) + I_y\left(\tfrac{4}{3}P_o - \tfrac{1}{3}P_2\right) \right\} d(\cos\theta)$$

$$+ \frac{2\pi n_e}{h} \int_{\sqrt{\frac{2h\nu}{m}}}^{\infty} v^3 dv f_m D\left(\frac{v}{v_{th}}\right) \int_0^{\pi} \left\{ I_x\left(\tfrac{2}{3}P_o + \tfrac{1}{3}P_2\right) + I_y\left(\tfrac{4}{3}P_o - \tfrac{1}{3}P_2\right) \right\} P_1 d(\cos\theta)$$

$$= \frac{8\pi}{3} I_{max} + 0 \ . \qquad (37)$$

since the P_ℓ's are orthogonal. Thus the Spitzer-Härm distribution and first order trapped particle corrections (Eq. 20) do not enhance a thermal spectrum (I_{max}) since the perturbation in the direction of the toroidal field ($\cos\theta > 0$) is produced at the expense of the distribution opposite the field ($\cos\theta < 0$). Any perturbation odd in $v_{||}$ does not alter a thermal spectrum.

An example of a non-thermal spectrum is shown in Fig. 17, which was taken during the steady state portion of a 60 kG, 160 kA discharge with a line-averaged density of $1.2\textcircled{14}\,\mathrm{cm}^{-3}$ and a loop voltage of 1.15 V. The open circles are points taken through a .05cm Be filter. The features between 5.5 and 7.0 keV are due to K radiation from chromium and iron. The lower curve is the expected spectrum from a 1250 eV thermal plasma with a Gaussian profile width of 6cm, predicted by Eq. 32. A "temperature" of 1900 eV would be obtained by fitting the points between 3.7 and 5.2 keV. The ratio E/E_r for this case, found from

$$\frac{E}{E_r} = \frac{ET_e}{\pi n e^3 \ln\Lambda} = 4.52\textcircled{10}\frac{V_1 T_e}{n_e \ln\Lambda} \qquad (38)$$

(with T_e in eV, V_1 in volts, and n_e in cm^{-3}), is equal to .028 if T_e is 1250 eV.

The contribution to a thermal spectrum from an even perturbation in θ, the second order term in the region II expansion of Kruskal and Bernstein (Eq. 17), may be computed from

$$I(h\nu) = \frac{8\pi}{3} I_{max} + \frac{2\pi n_e}{h} \int_{\sqrt{\frac{2h\nu}{m}}}^{\infty} v^3 dv f_m \left(\frac{E}{E_r}\right)^2 \left(\frac{v}{v_{th}}\right)^8 \chi$$

$$\int_0^{\pi} \left\{ I_x \left(\tfrac{2}{3}P_o + \tfrac{1}{3}P_2\right) + I_y \left(\tfrac{4}{3}P_o - \tfrac{1}{3}P_2\right) \right\} \left[\frac{P_o}{144} + \frac{P_2}{126}\right] d(\cos\theta) =$$

$$\frac{8\pi}{3} I_{max} + \frac{2\pi n_e}{h} \int_{\sqrt{\frac{2h\nu}{m}}}^{\infty} v^3 dv f_m \left(\frac{E}{E_r}\right)^2 \left(\frac{v}{v_{th}}\right)^8 \left\{ .0103 I_x + .0175 I_y \right\} . \qquad (39)$$

Substituting I_x'' and I_y'' from section II into Eq. 39, and performing the integrals, it is found that the contribution to the spectrum at 5.0 keV ($h\nu/T = 4$) is .6% and not the factor of 2 or so required to fit the data in Fig. 17. In this particular case, the contribution to the spectrum from the high velocity extension of the Spitzer-Härm (classical) distribution function is about a factor of 300 too small. This can be traced to the smallness of E/E_r and its coefficients. The conclusion here is that the classical electric field driven perturbation to the Maxwellian distribution function is unable to account for the observed x-ray spectrum in Alcator under certain conditions.

A convenient measure of the departure of the distribution from a Maxwellian is obtained by taking the ratio of T_t (defined as the "temperature" obtained by fitting the x-ray spectrum between 3.5 and 5.5 keV) to T_b (defined as the temperature predicted by Eq. 32). $\theta \equiv T_t/T_b = 1$ for a thermal plasma. For example, $\theta = 1.6$ for the case shown in Fig. 17, whereas for Fig. 11, $\theta = 1.07$. The only significant change between the two discharges is a factor of 3.5 in line averaged density. Alterations in plasma current also influence θ. Fig. 18 demonstrates the result of raising the current from 100 to 200 kA for a 60 kG discharge with $\bar{n} = 2.5\,(14)\,\mathrm{cm}^{-3}$. In both cases $V_1 = 1.7$ V and $T_b = 950$ eV. However, θ for the upper spectrum is 3.5 and for the lower spectrum is 1.25. Fig. 19 is a summary of 60 kG data which is a plot of θ vs. ξ ($\equiv 8\,(-4)\, I/n_o \sqrt{T_b}$). The curve is an empirical fit. It is apparent that the spectra become distinctly non-thermal when ξ is greater than some critical value around .03.

The radial dependence of this non-thermal behaviour is exhibited in Figs. 20 and 21 which are spectra taken along chords at $\pm$ 3.8 cm inside and outside (obtained from the top of the machine) and $\sim\pm$ 7.5 cm for the same discharges as in Fig. 17. The curves are the expected spectra at the corresponding radii for a thermal plasma with a central temperature of 1250 eV and a profile width of 6cm. The non-thermal tail increases dramatically with minor radius. θ at the center is 1.7, at $\pm$ 3.8 cm is 1.9 and at $\pm$ 7.5 cm is 3. Other data indicate that this tail is also symmetric up and down and increases with minor radius. That this non-thermal tail increases with minor radius has been noted on T-10[5] as well. This increase with minor radius is contrary to what one would expect from an electric field driven perturbation. For the discharge shown in Figs. 17, 20 and 21, E/E_r decreases with minor radius as shown in Fig. 22. Trapped electron effects, according to Eq. 22, would produce a smaller tail at the outside of the machine ($\cos\theta \sim 0$) which is not observed. If one takes the point of view that the current must be maintained at a certain level regardless of trapping, then, since there are more trapped electrons on the outside of the machine and thus fewer current carriers available, it is incumbent upon these fewer circulating electrons to increase their velocity to maintain the current. These higher velocity current carriers would then produce a larger x-ray tail on the outside of the machine, which is not observed. Vertical drift of fast electrons in the ripple of the magnetic field at the ports[27] is ruled out as a mechanism for producing the tail at large minor radii because of the observed up-down symmetry. If these fast electrons, which have drifted to larger radii, then scatter into trapped banana orbits, they would concentrate on the outside of the machine as observed on T-10[5]. However, this mechanism is only important for electrons with energy $\varepsilon > \varepsilon_d$[27] where

$$\varepsilon_d \approx \frac{e^2}{2}\left[\frac{8\pi(1+Z)RB\ln\Lambda_c\bar{n}\ell}{\sqrt{m}\,c\delta}\right]^{2/5} = 7.2\,\textcircled{-9}\left[\frac{R\bar{n}\ell\omega_{ce}\ln\Lambda_c}{\delta}\right]^{2/5}\text{eV} \qquad (40)$$

and where R is the major radius of the machine, $\bar{n}$ is the average density, ℓ is approximately the minor radius, ω_{ce} is the electron cyclotron frequency, δ is the field ripple at the port, $\Delta B/B$, $\ln\Lambda_c \equiv \ln\Lambda + \ln(4E_r/E)$, and all quantities are in cgs. Taking $B_T = 60$ kG, $\delta = .04$, $\ell = 5$cm, $\bar{n} = \textcircled{14}\,\text{cm}^{-3}$ and $E/E_r = .03$, one finds that this process is only important for $\varepsilon > 25$ keV and is not of interest here.

Another possible mechanism which could produce this non-thermal tail is interaction with "$\omega_{pe}\cos\theta$", electrostatic waves resonating with electrons with $v > v_{th}$. These waves could be produced[28] by the high energy ($\varepsilon > 100$ keV) electrons present in Alcator[29]. The production of a non-thermal tail on the electron distribution by $\omega_{pe}\cos\theta$ waves has been observed[30,31] under other circumstances. There is also a possible correlation of the x-ray tail and m = 2 oscillations under conditions of high current and low density[32].

In order to compute the energy confinement time for a given discharge, it is necessary to know the linear energy density of the plasma. This may be determined from

$$U \equiv \int_0^{a_L} 2\pi r dr \sum_i \int d\Omega \int_0^{\infty} v^2 dv f_i(\bar{v}) \tfrac{1}{2} m v^2 \tag{41}$$

where the sum is over the species present and poloidal and toroidal symmetry are assumed. For a Maxwellian distribution function, with $T_i = \alpha T_e$, Eq. 41 becomes

$$U = \tfrac{3}{2}(1+\alpha) \int_0^{a_L} n_e(r) T_e(r) 2\pi r dr \ . \tag{42}$$

If Gaussian density and temperature profiles are assumed, this integral may be performed analytically,

$$U = \tfrac{3}{2}(1+\alpha)\pi \frac{a^2 b^2}{a^2+b^2} n_o T_o \tag{43}$$

where $n_e(r) = n_o \exp -r^2/b^2$. The energy confinement time may then be found as the ratio between the linear energy density and the ohmic power delivered per unit length,

$$\tau_E \equiv \frac{U}{E\cdot I} = \frac{U2\pi R}{V_l I} = 25.6(1+\alpha)\frac{a^2b^2}{a^2+b^2}\,\frac{n_oT_o}{V_l I}\ \text{ms} \tag{44}$$

where now n_o is in ⑭ cm^{-3}, T_o is in keV, V_l is in V, I is in kA, and a and b are in cm.

For non-thermal discharges, an actual form for the distribution function (and radial dependence) must be used in Eq. 41. For simplicity in data analysis, consider the model distribution function (a bimaxwellian)

$$f(\bar{v}) = n_b f_{maxb} + n_t f_{maxt} \tag{45}$$

where f_{maxb} has temperature T_b and f_{maxt} has temperature T_t. As an example, for the spectrum of Fig. 17, a model distribution with $T_b = 1200$ eV, $T_t = 2000$ eV, and $n_t/n_b = .2$ would account for the data. The profile width, a, is 6 cm for both components. The average temperature, $\langle T\rangle$ ($\equiv T_bn_b/n + T_tn_t/n$), for this case is 1330 eV. $\langle T\rangle$ can be used for T_o in Eq. 44 to find τ_E. If a density profile width, b, of 8.5 cm is assumed and T_i is taken to be 710 eV, then the energy confinement time from Eq. 44 is ∿ 10 ms for this case, with an accuracy no greater than 20%. The above procedure for computing energy confinement times has been applied to a sequence of discharges at ∿ 145 kA and 60 kG with varying density. The results are shown in Fig. 23. The dashed curve is from the Thomson scattering experiment[1] and the solid curve is an empirical fit to the data. It is seen that the confinement time increases linearly with density over this range within the errors. It is interesting to note the apparent connection of this behaviour with the non-thermal tail on the x-ray spectra. Fig. 24 is a plot of θ^{-1} vs. density for the same discharges analyzed above. As the density is increased, the tail on the distribution disappears, and the energy confinement improves. This issue will be discussed in the next section.

In summary, under conditions of high current and low density, the classical theory of the electron distribution function, to second order in E/E_r, including the effects of trapped electrons, is unable to account for the observed x-ray spectra. The appearance of this non-classical tail is correlated with the decrease in energy confinement time. This non-thermal behaviour increases with minor radius with poloidal symmetry.

VI. Kinetic Diffusion Equation Solution

With formally making the connection between non-thermal distributions and poor energy confinement in mind, consider the following electron kinetic equation which incorporates the effects of spatial diffusion[33],

$$\frac{\partial f_e}{\partial t} = C(f_e) - \frac{e}{M}\bar{E} \cdot \bar{\nabla}_v f_e + \mathcal{L} r^2 \hat{D} \mathcal{L} f_e \qquad (46)$$

where $\bar{E}$ is the externally applied electric field and C is the collision operator. $\mathcal{L}$ is assumed to be (in cylindrical coordinates) $\frac{v_\parallel}{r}\left(\frac{\partial}{\partial r} - \frac{eE_A}{m}\frac{\partial}{\partial w}\right)$ where $w = v^2$ and E_A is the ambipolar electric field produced from the charge separation caused by the electron diffusion, and $\hat{D}$ is assumed to have the form $\frac{D_o(r)}{|v_\parallel|\, r}$. The steady state solution to Eq. 46 can be obtained from an expansion in powers of E/E_r ($f_e = f_o + f_1 + f_2 + \ldots$), where $D_o(r)$ is regarded as second order since the diffusive loss process must balance ohmic heating which is second order.

The collision operator in the zeroth order equation requires $f_e = f_o$ to be a local Maxwellian. The first order equation is

$$0 = C(f_1) - \frac{e}{m}\bar{E} \cdot \bar{\nabla}_v f_o \qquad (47)$$

and the distribution and electrical conductivity are given by Eqs. 11 and 13 respectively. The second order equation is

$$0 = C(f_2) - \frac{e}{m}\bar{E} \cdot \bar{\nabla}_v f_1 + \mathcal{L}\frac{rD_o}{|v_\parallel|}\mathcal{L} f_o \,. \qquad (48)$$

In order for particle number to be conserved, the ambipolar field must draw inward the same number of electrons that diffuse outward. The equation of constraint for the field may be found from the particle moment of Eq. 48,

$$\pi\int_{0}^{\infty}\sqrt{w}\;dw\int_{-1}^{1}d\mu\;L\,\frac{rD_{o}(r)}{|v_{||}|}\;Lf_{o} = 0. \tag{49}$$

Insertion of Eq. 9 for f_o into Eq. 49 yields a Riccati equation for E_A,

$$\varepsilon^{2}+\frac{\partial\varepsilon}{\partial r}+(2\alpha_{n}+\alpha_{D_{o}})\,\varepsilon+\alpha^{2}+\frac{\partial\alpha}{\partial r}+\alpha\alpha_{D_{o}} = 0 \tag{50}$$

where $\varepsilon(r) \equiv \frac{eE_{A}(r)}{2T_{e}(r)}$, $\alpha \equiv \alpha_{n}+\frac{1}{2}\alpha_{T}$, $\alpha_{n} \equiv \frac{\partial \ln n}{\partial r}$, $\alpha_{T} \equiv \frac{\partial \ln T}{\partial r}$ and $\alpha_{D_{o}} \equiv \frac{\partial \ln D_{o}}{\partial r}$. This first order, non-linear equation for $\varepsilon(r)$ may be transformed to a second order, linear equation by making the substitution $\varepsilon \equiv \frac{\partial \ln U}{\partial r}$,

$$\frac{\partial^{2}U}{\partial r^{2}} + (2\alpha_{n}+\alpha_{D_{o}})\,\frac{\partial U}{\partial r} + \left(\alpha^{2}+\frac{\partial\alpha}{\partial r}+\alpha\alpha_{D_{o}}\right)U = 0. \tag{51}$$

Once the appropriate profiles are known, this equation may be solved for $E_A(r)$. In order to visualize a realistic behaviour for $E_A(r)$, consider a situation with $n(r) = n_o \exp-(r^2/b^2)$, $T(r) = T_o \exp-(r^2/a^2)$, and $\alpha_{D_o} = 0$. The solution, utilizing the boundary condition $E_A(0) = 0$, is

$$E_{A}(r) = \frac{T_{o}e^{-r^{2}/a^{2}}}{e}\left(\frac{1}{b^{2}}+\frac{1}{2a^{2}}\right)\left\{4r-\frac{8}{3}\,\frac{r^{3}}{a^{2}}+\frac{8}{15}\,\frac{r^{5}}{a4}+\ldots\right\}. \tag{52}$$

From this the ambipolar potential may be found, $\phi(r) = \int_o^r E_A(r)\,dr$. The ratio of the potential energy a diffusing electron gains in this electric field to the local value of the temperature is,

$$\frac{e\phi(r)}{T(r)} = \frac{13}{15}\left(1 + \frac{2a^2}{b^2}\right)\left\{e^{r^2/a^2} - 1 + \frac{2}{13}\,\frac{r^2}{a^2} - \frac{4}{13}\,\frac{r^4}{a^4} + \ldots\right\}, \tag{53}$$

and is shown in Fig. 25 for the case a = 6cm and $2a^2 = b^2$. It is seen that the ambipolar potential is as large as the temperature only 4cm from the center of the plasma. The importance of this potential in the kinetic equation may be estimated by comparing terms in the diffusion operator,

$$Lf_o = \frac{v_\parallel}{r}\left\{\alpha_n - \frac{3}{2}\,\alpha_T + \frac{v^2}{v_{th}^2}\,\alpha_T + \varepsilon\right\} f_o \tag{54}$$

and substituting from Eq. 52, it is found that the ambipolar field may be ignored if $(v/v_{th})^2 >> r/7.4\text{cm})^2$. This neglect is appropriate for most radii in the plasma as far as the soft x-ray spectrum is concerned which involves electrons with $(v/v_{th})^2 \geq 4$.

The energy moment of Eq. 48,

$$\frac{\pi m}{2}\int_{-1}^{1} d\mu \int_{o}^{\infty} w^{3/2}\,dw \left\{ L\,\frac{rD_o}{|v_\parallel|}\quad Lf_o - \frac{e}{m}\,\bar{E}\cdot\bar{\nabla}_v f_1 \right\} = 0 \tag{55}$$

yields the heat transport equation (after substitution of Eq. 50)

$$0 = \vec{E}\cdot\vec{j} + \frac{2}{\sqrt{\pi}}\,\frac{v_{th}D_o}{r}\left\{\frac{n\partial^2 T}{\partial r^2} + \frac{\partial T}{\partial r}\left(\frac{n}{T}\,\frac{\partial T}{\partial r} + \frac{2\partial n}{\partial r} + 2n\varepsilon + n\alpha_{D_o}\right)\right\} \tag{56}$$

where $\vec{j} = e \int \vec{v}\, f_1\, d\overline{v}$.

From this the overall power balance equation may be obtained by integrating over the plasma cross section,

$$IE = 2\pi D_o n_o T_o v_{th_o} \; \frac{2}{a} 2^{3/2} \frac{\left(1 + \frac{2a^2}{b^2}\right)}{\left(3 + \frac{2a^2}{b^2}\right)^{3/2}} \; , \tag{57}$$

where, again, it is assumed that $\alpha_n = - 2r/b^2$, $\alpha_T = - 2r/a^2$, $\alpha_{Do} = 0$, and, from Eq. (52), $\varepsilon \simeq - \alpha_n - \frac{\alpha_T}{2}$. This is to be compared with Eq. (43). There remains to solve the kinetic equation (48).

The response to an electric field has already been provided (Eq. 17) so it will be sufficient to demonstrate the effects of the diffusion term,

$$C(f_2) = - L \; \frac{rD_o}{|v_\parallel|} \; L\, f_o \; . \tag{58}$$

This may be written in the high velocity approximation ($u^2 \equiv 2(v/v_{th})^2 >> 1$) as

$$\frac{\nu}{u^3} \frac{\partial}{\partial \mu}(1-\mu^2) \frac{\partial}{\partial \mu} f_2 + \frac{\nu}{u^2} \frac{\partial}{\partial u}\left(f_2 + \frac{1}{u} \frac{\partial f_2}{\partial u}\right) = - |\mu| \frac{v_{th}}{r} \frac{D_o \alpha_T^2}{4\sqrt{2}} u^5 f_o \tag{59}$$

where ν is the collision frequency $\simeq 3.87$ (-6) $\ln\Lambda n/T^{1.5}\ \mathrm{sec}^{-1}$, with T_e in eV and n in cm^{-3}. If f_2 is written $f_oP^2(u,\mu)$, this becomes,

$$\frac{\partial}{\partial\mu}(1-\mu^2)\frac{\partial}{\partial\mu}P^2 - \frac{u\partial P^2}{\partial u} = -|\mu|\,u^8\,\frac{v_{th}D_o}{r\nu 4\sqrt{2}}\,\alpha_T^2 \,. \tag{60}$$

This equation may be solved by expanding P^2 in Legendre polynomials

$$P^2 = \sum_m g_m(u)P_m(\mu) \tag{61}$$

and noting that

$$|\mu| = \sum_m a_m P_m(\mu) \equiv \sum_m \left(\frac{2m+1}{m+2}\right)\left[P_{m-2}(0) + P_m(0)\right]P_m(\mu) \tag{62}$$

where $P_{-2}(0) = 0$. Eq. (60) now becomes

$$m(m+1)g_m(u) + \frac{u\partial g_m(u)}{\partial u} = a_m\,u^8\,\frac{v_{th}D_o\alpha_T^2}{4\sqrt{2}r\nu} \tag{63}$$

which may be solved for $g_m(u)$

$$g_m(u) = \frac{a_m}{8 + m(m+1)}\,u^8\,\frac{v_{th}D_o\alpha_T^2}{r\nu 4\sqrt{2}} \,. \tag{64}$$

Finally, the $u^2 >> 1$ expression for the distribution function is

$$f_e = \frac{n(r)}{\pi^{3/2} v_{th}^3(r)} \, e^{-\frac{v^2}{v_{th}^2(r)}} \left\{ 1 + \frac{v_{th}(r)\; D_o(r)\,\alpha_T^2(r)}{r\nu(r)\sqrt{2}} \left(\frac{v}{v_{th}(r)} \right)^8 \left[\frac{1}{4} P_o + \frac{5}{28} P_2 - \frac{9}{336} P_4 + \ldots \right] \right\} \quad . \qquad (65)$$

To second order in $D_o(r)$ this becomes[34]

$$f_e = f_m \left\{ 1 + \frac{v_{th} D_o \alpha_T^2}{r\nu\sqrt{2}} \left(\frac{v}{v_{th}} \right)^8 \left[\frac{1}{4} P_o + \frac{5}{28} P_2 \right] + \left(\frac{v_{th} D_o \alpha_T^2}{r\nu\sqrt{2}} \right)^2 \left(\frac{v}{v_{th}} \right)^{16} \left[.037 P_o + .047 P_2 \right] \right\} . \qquad (66)$$

In summary, inclusion of a diffusion operator in the kinetic equation allows one parameter, $D_o(r)$, to govern departures from thermal distributions (66) and overall energy balance (57).

VIII. Determination of the Diffusion Coefficient

The X-ray spectrum from the distribution function Eq. (66) may now be calculated by insertion in Eq. (6) followed by integration over the profiles (in a similar fashion to Eq. (28). The free parameters, $T_e(r)$ and $D_o(r)/r$, may then be adjusted to fit the spectrum. As an example of the employment of this technique, consider the spectra in Fig. 26. For the selection $T_e(r) = T_o \exp(-r^2/a^2)$ with $T_o = 1000$ eV and $a = 6$ cm, and $D_o(r) = h_o r \exp(-r^2/c^2)$ with $h_o =$ 1.3 (-4) cm and $c = 2.68$ cm, the predicted spectra are shown in Fig. 26. The agreement is quite good supporting this particular selection of a gaussian for the diffusion coefficient. $D_o(r)$ and $T(r)$ are shown in Fig. 27 for comparison. This technique has been applied to the same sequence of discharges as in section VII ($I = 145$ kA, $B = 60$ kG, $1 \leq \bar{n} \leq 6$ ⑭ cm^{-3}). The outcome is depicted in Figs. 28 and 29, which indicate the density dependence of h_o. It is seen that h_o decreases with rising density, perhaps as $\bar{n}^{-1}$. Fig. 29 should be compared with Fig. 24. This behavior provides the following scenario. As the density is increased, the diffusion coefficient is reduced, and the energy confinement improves in conjection with the decline in the non-thermal component of the X-ray spectra. In other words, the energy confinement time, τ, increases with density,

$$\tau \sim \left[\frac{v_{th} D_o(r)}{r} \alpha_T^2\right]^{-1} \propto \frac{1}{h_o} \propto n \,. \tag{67}$$

The dependence of h_o on current may be deduced from the discharges shown in Fig. 18. The results are demonstrated in Fig. 30 in addition to those from a sequence of shots of varying current at $\bar{n} = 3.3$ ⑭ cm^{-3}. The point which is an estimate is from Fig. 28.

The dependence on current is perhaps stronger than $\propto I$. Information concerning the reliance of h_o on the toroidal magnetic field may be extracted from two discharges with $I = 145$ kA and $n = 2.8$ $\textcircled{14}$ cm^{-3} with $B_T = 60$ and 40 kG. h_os for these cases were 6 $\textcircled{-4}$ and 5 $\textcircled{-4}$ cm, respectively, not substantially different. Any dependence of the diffusion coefficient on the toroidal field is weak and may only enter as a reflection of profile changes, not through any explicit dependence.

The indication is that the diffusion is driven by the plasma current and inhibited by high densities. There remains to address the question of energy balance.

Consider the case with $D_o(r) = rh_o \exp(-r^2/c^2)$, hence $\alpha_{Do} = (1 - 2r^2/c^2)/r$. Before inserting this in the heat transport equation (56), the effect of this choice for $D_o(r)$ on the ambipolar electric field must be demonstrated. Using this form for α_{Do} in Eq. (51), it is found that

$$\varepsilon = 2r\left(\frac{1}{b^2} + \frac{1}{2a^2}\right) + r^3\left[\frac{2}{b^2c^2} - \frac{1}{b^2a^2} - \frac{1}{2a^4}\right] \tag{68}$$

which to lowest order in r is the same as Eq. (52). The precise shape of the function $D_o(r)$ does not affect the ambipolar field at small radii. Insertion of α_{Do} into Eq. (56) and integration over the plasma cross section produces the new power balance equation,

$$IE = 8\sqrt{\pi}\, v_{tho}\, n_o\, T_o\, h_o \frac{\left(\frac{1}{2} + \frac{a^2}{b^2}\right)}{\left(\frac{3}{2} + \frac{a^2}{b^2} + \frac{a^2}{c^2}\right)^2} \tag{69}$$

to be contrasted with Eq. (57). In more practical form, this becomes,

$$\frac{IV}{.339} = 13500\ T_o^{3/2}\ n_o h_o \frac{\left(\frac{1}{2} + \frac{a^2}{b^2}\right)}{\left(\frac{3}{2} + \frac{a^2}{b^2} + \frac{a^2}{c^2}\right)^2}\quad \frac{\text{amp-volt}}{\text{cm}} \qquad (70)$$

with I in kA, V in volts, T_o in eV, n_o in ⑭ cm^{-3}, and h_o in cm. Symbolically, power in = power out. This equation is plotted in Fig. 31 for all the cases just discussed. The curve indicates power balance. The major drawback in this figure is that some of the points lie well above the curve, indicating that more energy is coming out of the plasma than went in. This is clearly inaccurate. These are from the spectra with the largest non-thermal tails, and the h_os required to account for these tails require too large an outward heat flux. The source of the problem is probably the kinetic equation solution, the distribution function Eq. (66). When the departures from the maxwellian become large, the validity of the perturbative expansion for the distribution function is suspect.

In summary, evidence has been presented supportive of a kinetic equation of the form in Eq. (46) to be valid in Alcator under certain conditions. X-ray spectra and overall power balance are simultaneously accounted for and the formal connection between non-thermal distributions and poor energy confinement has been demonstrated. The diffusion coefficient, $D_o(r)/r$, is found to vary spatially as h_o $\exp(-r^2/c^2)$, and scales roughly as I/n with a weak dependence on toroidal magnetic field. This indicates that energy confinement should increase with density. Even though the diffusion coefficient increases with current, the global energy confinement is not necessarily degraded because the profiles broaden and the volume of contained hot plasma increases.

There remains to find a source for the kinetic diffusion equation (46) and the scalings of the diffusion coefficient.

IX. Random Radial Magnetic Fields as the Origin of the Diffusion

Assume that there is a random radial magnetic field, $\tilde{B}$, superimposed on the confining toroidal field B_T. Electrons, which at a given toroidal location sample this field every revolution, undergo a random radial walk with step size Δr, such that $\Delta r/2\pi R = \tilde{B}/B_T$. The time between steps is just the time to transit the machine, $\Delta t = 2\pi R/|v_\parallel|$. From this one may construct a diffusion coefficient,

$$D = \frac{(\Delta r)^2}{\Delta t} = 2\pi R|v_\parallel|\left(\frac{\tilde{B}}{B_T}\right)^2 . \tag{71}$$

If this is the mechanism causing the diffusion of electrons described in the last two sections, then the magnitude of $\tilde{B}$ may be found from Eq. (71) and the diffusion coefficient determined from the x-ray spectra. Assuming this process is most important for electrons with $v_\parallel \sim 4\ v_{th}$, and taking a typical value for $D/v_{th} = h_o$, say $1.5\ \textcircled{-5}$ cm, then it is found that $\tilde{B}/B_T \sim \textcircled{-4}$. Fluctuating field of this size have been seen in Macrotor.[35] The size of the random radial magnetic field required to distort the distribution function and provide the anomalous electron heat loss is indeed small, of order .01% of the toroidal field.

Consider a more formal derivation of Eqs. (71) and (46). The starting point is the zero Larmor radius drift kinetic equation, (in cylindrical coordinates)

$$\frac{\partial f_e}{\partial t} + v_\parallel\ \vec{b} \cdot \vec{\nabla} f_e = 0 \tag{72}$$

where it is assumed that $\vec{b} = \vec{b}_o + \tilde{\vec{b}}$, where $\vec{b}_o$ is the unit vector in the direction of the external field (toroidal and poloidal), and

$$\tilde{\vec{b}} = \sum_{m,n} \tilde{\vec{b}}_{mn}(r)\; e^{\,j(m\Theta - n\phi)} \qquad (73)$$

is a random radial component. Assume also that $\vec{\nabla} \cdot \tilde{\vec{b}} = 0$, define the Θ and ϕ average

$$< \; > \equiv \frac{1}{(2\pi)^2} \int_{-\pi}^{\pi} d\Theta \int_{-\pi}^{\pi} d\phi \qquad (74)$$

and seek a solution of the form $f_e = \bar{f} + \tilde{f}$, where $\bar{f}$ is independent of Θ and ϕ and $\tilde{f}$ is small (order $\tilde{b}$). Application of $< \; >$ to Eq. (72) yields

$$\frac{\partial \bar{f}}{\partial t} + v_{\|} < \tilde{\vec{b}} \cdot \nabla \tilde{f} > = 0 \qquad (75)$$

and

$$\frac{\partial \tilde{f}}{\partial t} + v_{\|}\, \vec{b} \cdot \nabla \tilde{f} - v_{\|} < \tilde{\vec{b}} \cdot \nabla \tilde{f} > + v_{\|}\, \tilde{\vec{b}} \cdot \overline{\nabla f} = 0 \; . \qquad (76)$$

If now $\bar{f}$, $\tilde{f}$, and $\frac{\partial}{\partial t}$ are expanded in powers of $\tilde{b}$,

$$\bar{f} = \bar{f}^0 + \bar{f}^1 + \ldots , \quad \tilde{f} = \tilde{f}^1 + \tilde{f}^2 + \ldots , \quad \frac{\partial}{\partial t} = \frac{\partial}{\partial t_0} + \frac{\partial}{\partial t_1} + \frac{\partial}{\partial t_2} + \ldots \qquad (77)$$

Eq. (75) may be solved order by order. The zeroth order equation is $\partial\bar{f}^0/\partial t_o = 0$.

At first order,

$$\frac{\partial\bar{f}^0}{\partial t_1} + \frac{\partial\bar{f}^1}{\partial t_o} = 0 \ . \tag{78}$$

In order for $\bar{f}^1 = -\int dt_o \ \partial\bar{f}^0/\partial t_1$ not to grow without bound on the t_o time scale, $\partial\bar{f}^0/\partial t_1$ is required to vanish, which implies $\partial\bar{f}^1/\partial t_o = 0$. The second order equation is

$$\frac{\partial\bar{f}^0}{\partial t_2} + \frac{\partial\bar{f}^1}{\partial t_1} + \frac{\partial\bar{f}^2}{\partial t_o} + < v_{\parallel} \ \tilde{\bar{b}} \cdot \nabla \ \tilde{f}^1 > = 0. \tag{79}$$

$\bar{f}^2$ will depend on t_o unless

$$\frac{\partial\bar{f}^0}{\partial t_2} + \frac{\partial\bar{f}^1}{\partial t_1} + < v_{\parallel} \ \tilde{\bar{b}} \cdot \nabla\tilde{f}^1 >_{\text{sec}} = 0 \simeq \frac{\partial\bar{f}^0}{\partial t_2} + < v_{\parallel} \ \tilde{\bar{b}} \cdot \nabla\tilde{f}^1 >_{\text{sec}} \tag{80}$$

where the subscript sec denotes t_o independence. To calculate $\tilde{f}^1$, write Eq. (76) to first order,

$$\frac{\partial\tilde{f}^1}{\partial t_o} + v_{\parallel} \ \bar{b} \cdot \nabla\tilde{f}^1 + v_{\parallel} \tilde{\bar{b}} \cdot \overline{\nabla f}^0 = 0 \tag{81}$$

which may be integrated along the exact orbit

$$\tilde{f}^1 = - v_\parallel \int_0^{t_o} dt' \, \tilde{\vec{b}} \cdot \overline{\nabla f^0} \Big|_{\text{exact orbit}} . \qquad (82)$$

The exact orbit equations are

$$\begin{aligned} r(t) &= r_o + \delta r \\ \phi(t) &= \phi_o - \frac{v_\parallel t}{2\pi R} + \delta\phi \\ \Theta(t) &= \Theta_o - \frac{v_\parallel t}{2\pi R\, q} + \delta\Theta \end{aligned} \qquad (83)$$

with $\delta\Theta \simeq - \delta\phi/q$ where q is the safety factor. Eq. (80) may now be written, (in cylindrical coordinates) using Eq. (82).

$$\frac{\partial \overline{f}_o}{\partial t_2} = - < \frac{v_\parallel}{r} \frac{\partial}{\partial r} \left(r\tilde{b}_r \tilde{f}^1 \right) >_{\text{sec}} = < \frac{v_\parallel^2}{r} \frac{\partial}{\partial r} \left(r\tilde{b}_r \int_0^{t_o} dt' \tilde{\vec{b}} \cdot \overline{\nabla f_o} \Big|_{\substack{\text{exact} \\ \text{orbit}}} \right) >_{\text{sec.}} \qquad (84)$$

Recalling Eq. (73) and the exact orbits, this becomes

$$\frac{\partial \overline{f}_o}{\partial t_2} = < \frac{v_\parallel^2}{r} \frac{\partial}{\partial r} r \sum_{\substack{m,n \\ m',n'}} \tilde{b}_{r_{mn}}(r) \int_0^{t_o} dt' \, \tilde{\vec{b}}_{m'n'}(r+\delta r) e^{j(m+m')\Theta - j(n+n')\phi} \qquad (85)$$

$$e^{j(n'-\frac{m'}{q})\frac{v_\parallel t'}{2\pi R}} e^{j\delta\Theta(m'+nq')} \cdot \overline{\nabla} f_o >_{\text{sec}} .$$

Taking the secular part, i.e., letting $t_o \rightarrow \infty$, and neglecting variations of $\tilde{\vec{b}}_{m'n'}(r + \delta r)$ and $\overline{f}_o$ over the δr distance scale, Eq. (85) evolves to

$$\frac{\partial \bar{f}^{0}}{\partial t_{2}} = \frac{v_{\parallel}}{r}\frac{\partial}{\partial r} r^{2} \sum_{\substack{m,n\\ m',n'}} \tilde{b}_{r_{mn}} \tilde{b}_{r_{m'n'}} \int_{0}^{\infty} dt' \left< e^{j(m+m')\Theta - j(n+n')\phi} \; e^{j\delta\Theta(m'+n'q)} \right> e^{j\left(n'-\frac{m'}{q}\right)\frac{v_{\parallel} t'}{2\pi R}} \frac{v_{\parallel}}{r}\frac{\partial}{\partial r} \bar{f}^{0} \quad . \tag{86}$$

$$\approx \frac{v_{\parallel}}{r}\frac{\partial}{\partial r} r^{2} \sum_{m,n} |\tilde{b}(r)_{m,n}|^{2} \frac{2\pi R}{|v_{\parallel}|} \mathcal{R}\left\{ \left(n-\frac{m}{q}\right), \delta\Theta \right\} \frac{v_{\parallel}}{r}\frac{\partial}{\partial r} \bar{f}^{0}$$

where $\mathcal{R}$ is some resonance function that depends on the details of the orbit $\delta\Theta$. This may be written in the form of a diffusion equation

$$\frac{\partial \bar{f}^{0}}{\partial t} = L r^{2} \hat{D} \quad L \bar{f}^{0} \tag{87}$$

where $\hat{D} = \sum_{m,n} |\tilde{b}_{mn}|^{2} \frac{2\pi R}{|v_{\parallel}|} \mathcal{R}\{(n - m/q), \delta\Theta\}$ and $L = \frac{v_{\parallel}}{r}\frac{\partial}{\partial r}$.

In the units of a diffusion coefficient, $D = 2\pi R |v_{\parallel}| \sum_{m,n} \mathcal{R}\{(n - m/q), \delta\Theta\} |\tilde{b}_{mn}|^{2}$, in agreement with Eq. (71). Eq. (87) becomes Eq. (46) when the collision operator and the toroidal electric field term are retained and an ambipolar piece is added to the L operator to conserve particle number. Finally, one has

$$\tilde{b}^2 \sim \sum_{m,n} |\tilde{b}_{mn}|^2 \; R\left\{\left(n-\frac{m}{\bar{q}}\right),\ \delta\Theta\right\} = \frac{h_o(r)}{2\pi R} \tag{88}$$

in agreement with earlier estimates. Section VIII provides the scalings of the fluctuating magnetic field level with electron density, current, and toroidal field.

X. Conclusions

Under normal operating conditions in Alcator, the electron distribution function is Maxwellian. The central electron temperature may then be determined from macroscopic parameters (the toroidal field, loop voltage, Z_{eff}, and the central safety factor),

$$T_o = 84\ \text{eV}\left(\frac{B_T}{V_l}\right)^{2/3}\left(\frac{Z_{eff}}{q_o}\right)^{2/3} \simeq 90\ \text{eV}\left(\frac{B_T}{V_l}\right)^{2/3} \qquad (89)$$

with B_T in kG, V_l in volts, consistent with $Z_{eff} = 1$ and $q_o = .9$. If the temperature profile shape is Gaussian, the width, a, may be found from

$$a = 3.8\ \text{cm}\sqrt{\frac{I}{B_T}} \qquad (90)$$

with I in KA and B_T in kG.

When 8.0 (-4) $I/n_o\sqrt{T_o} > .03$ (with I in kA, n_o in (14) cm^{-3} and T_o in keV) the X-ray spectrum becomes distinctly non-thermal. This effect cannot be explained by classical electric field driven perturbation theory, even with E/E_r as large as 3%. This non-classical tail increases with I/n and minor radius, is symmetric both up and down, in and out, and may be correlated with poor energy confinement (anomalous electron heat loss).

This correlation is formalized by the inclusion of a spatial diffusion term in the electron kinetic equation. The diffusion coefficient appears in both the power balance equation and the perturbation to the electron distribution function. The values of the diffusion coefficient determined from the non-thermal x-ray spectra satisfy the power balance equation, justifying the assumed kinetic diffusion equation. The diffusion coefficient, D, scales as 1/n and hence the energy confinement time, τ, (which is inversely proportional to D) is proportional to n. The diffusion coefficient is peaked on axis. A possible source for the kinetic diffusion equation is the inclusion of the effects of a random radial magnetic field. The required level of magnetic fluctuation $\Delta B/B$ is $\sim$ (-4) .

XI. Acknowledgements

Thanks are due to many people who have contributed to this work in various ways, particularly Ron Parker, Dave Overskei, Ian Hutchinson, and Bruno Coppi.

REFERENCES

1. M. Gaudreau et. al., Phys. Rev. Lett. 39, 1266 (1977).
2. S. von Goeler et. al., Nuc. Fus. 15, 301 (1975).
3. S. Sesnic, Pulsator Report IPP III/22 (1976).
4. Equipe TFR, Nuc. Fus. 17, 213 (1977).
5. A. V. Gurevich et. al., Pls'ma Zh. Eksp. Teor. Fiz. 26 (No. 11), 733 (1977).
6. A. Sommerfeld, Ann. d. Phys. [5] 11, 257 (1931).
7. R. Weinstock, Phys. Rev. 61, 585 (1942).
8. A. Sommerfeld and A. Maue, Ann. d. Phys. [5] 23, 589 (1935).
9. J. Greene, Ap. J. 130, 693 (1959).
10. W. Karzas and R. Latter, Ap. J. Supp. 6, 167 (1961).
11. P. Kirkpatrick and L. Wiedmann, Phys. Rev. 67, 321 (1945).
12. D. Menzel and C. Pekeris, M.N.R.A.S. 96, 77 (1935).
13. P. Brussaard and H. van de Hulst, Rev. Mod. Phys. 34, 507 (1962).
14. J. Terry et. al., Nuc. Fus. 18, 485 (1978).
15. M. Mattioli, EUR-CEA-FC-761 (1975).
16. C. Breton et. al., EUR-CEA-FC-948 (1978).
17. C. Moore, NBS circular 467 (1958).
18. R. Cohen, L. Spitzer and P. Routly, Phys. Rev. 80, 230 (1950).
19. L. Spitzer and R. Härm, Phys. Rev. 89, 977 (1953).
20. M. Kruskal and I. Bernstein, PPPL MATT Report Q-20, 174 (1962).
21. M. Rosenbluth, R. Hazeltine and F. Hinton, Phys. Fl. 15, 116 (1972).
22. B. Coppi, MIT RLE Report 7527 (1975).

23. J. E. Rice et. al, Phys. Rev. A 22, 310 (1980).

24. D. Overskei et. al., Int. Conf. on Solids and Plasmas in High Magnetic Fields, MIT (1978).

25. I. Hutchinson, private communication (1978).

26. A. Gondhalekar, private communication (1977).

27. A. V. Gurevich and Ya. S. Dimant, Nuc. Fus. 17, 629 (1978).

28. K. Molvig, M. Tekula and A. Bers, Phys. Rev. Lett. 38, 1404 (1977).

29. S. Kissel, H. Helava and J. Rice, Bull. Am. Phys. Soc. 22, 1147 (1977).

30. M. Porkolab, V. Aranasalam and R. Ellis, Phys. Rev. Lett. 29, 1438 (1972).

31. M. Porkolab, Physica 82C, North Holland; 86 (1976).

32. D. Overskei, private communication (1979).

33. K. Molvig, J. E. Rice, and M. S. Tekula, Phys. Rev. Lett., 41, 1240 (1978).

34. M. Tekula, private communication (1978).

35. S. J. Zweben, C. R. Menyuk, and R. J. Taylor, Phys. Rev. Lett. 42, 1270 (1979).

FIGURE CAPTIONS

Fig. 1. The average Gaunt factor, $\bar{g}$, as a function of photon energy for three different values of T_e, and the approximation $\bar{g} = (T/h\nu)^{1/3}$.

Fig. 2. The bremsstrahlung collision geometry.

Fig. 3. I_y, the y component of the bremsstrahlung cross section, as a function of photon energy for two values of the incoming electron energy, ε_o, and the analytic approximation $I_y^{\parallel}$.

Fig. 4. The thermal bremsstrahlung spectrum from Eq. 4 and Eq. 6 with the approximations for $I_x^{\parallel}$ and $I_y^{\parallel}$.

Fig. 5. The bremsstrahlung spectrum and the recombination enhancement spectrum from a .17% oxygen contamination.

Fig. 6. The Maxwellian electron distribution function (Eq. 9) and the Spitzer-Härm perturbation (Eq. 11) with $E/E_r = .05$.

Fig. 7. The Spitzer-Härm (Eq. 11) and Kruskal-Bernstein (Eq. 17) perturbations for $E/E_r = .05$.

Fig. 8. Toroidal geometry.

Fig. 9. The geometry of the detection system.

Fig. 10. Calculated bremsstrahlung spectra integrated along a chord 2 cm. from the plasma center for 3 different Gaussian temperature profile widths.

Fig. 11. An observed thermal X-ray spectrum and the calculated spectrum for an 850 eV plasma.

Fig. 12. An up-down radial temperature profile with n_e = 4.0 ⑭ cm^{-3}, I = 140 kA, and B_T = 60 kG.

Fig. 13. The temperature profile for $\bar{n}_e$ = 3.7 ⑭ cm^{-3}, I = 220 kA, and B_T = 60 kG. Data from Thomson scattering and electron cyclotron emission are shown for comparison.

Fig. 14. The central electron temperature as a function of (B_T/V_l) along with Eq. 32.

Fig. 15. The Gaussian temperature profile width as a function of (I/B_T) along with Eq. 33.

Fig. 16. The electron temperature profile width as a function of $I/n\sqrt{T}$ (v_d/vth).

Fig. 17. A non-thermal spectrum for a plasma with I = 160 kA and $\bar{n}_e$ = 1.2 ⑭ cm^{-3}. The lower curve is a 1250 eV thermal spectrum predicted by Eq. 32 and the upper curve is the best fit "temperature" of 1900 eV.

Fig. 18. Two spectra with $\bar{n}_e = 2.5$ ⑭ cm^{-3} and $V_e = 1.7\mathrm{V}$. The upper spectrum has I = 200 kA, in the lower spectrum, I = 100 kA.

Fig. 19. The parameter Θ, which measures the size of the non-thermal distribution, as a function of I/n.

Fig. 20. Non-thermal spectra from ±3.8 cm for discharges similar to Fig. 17. The curve is the predicted spectrum at 3.8 cm for T_e = 1250 eV at the center.

Fig. 21. Non-thermal spectra from $\sim$ ±7.5 cm for discharges similar to Fig. 17. The curve is the predicted spectrum at 7.5 cm for T_e = 1250 eV at the center.

Fig. 22. E/E_r as a function of radius.

Fig. 23. The energy confinement time from Eqs. 44 and 45 as a function of density, derived from X-ray spectra.

Fig. 24. The non-thermal parameter, Θ, as a function of density.

Fig. 25. The ratio of the ambipolar potential to the electron temperature as a function of radius.

Fig. 26. Non-thermal spectra at 0 and 4 cm with the best fit using the non-thermal electron distribution from Eq. 66.

Fig. 27. The model diffusion coefficient as a function of radius.

Fig. 28. The amplitude of the diffusion coefficient as a function of density.

Fig. 29. The amplitude of the diffusion coefficient as a function of density.

Fig. 30. The amplitude of the diffusion coefficient as a function of current.

Fig. 31. The power flowing out of the plasma as a function of the input ohmic power as determined from Eq. 70.

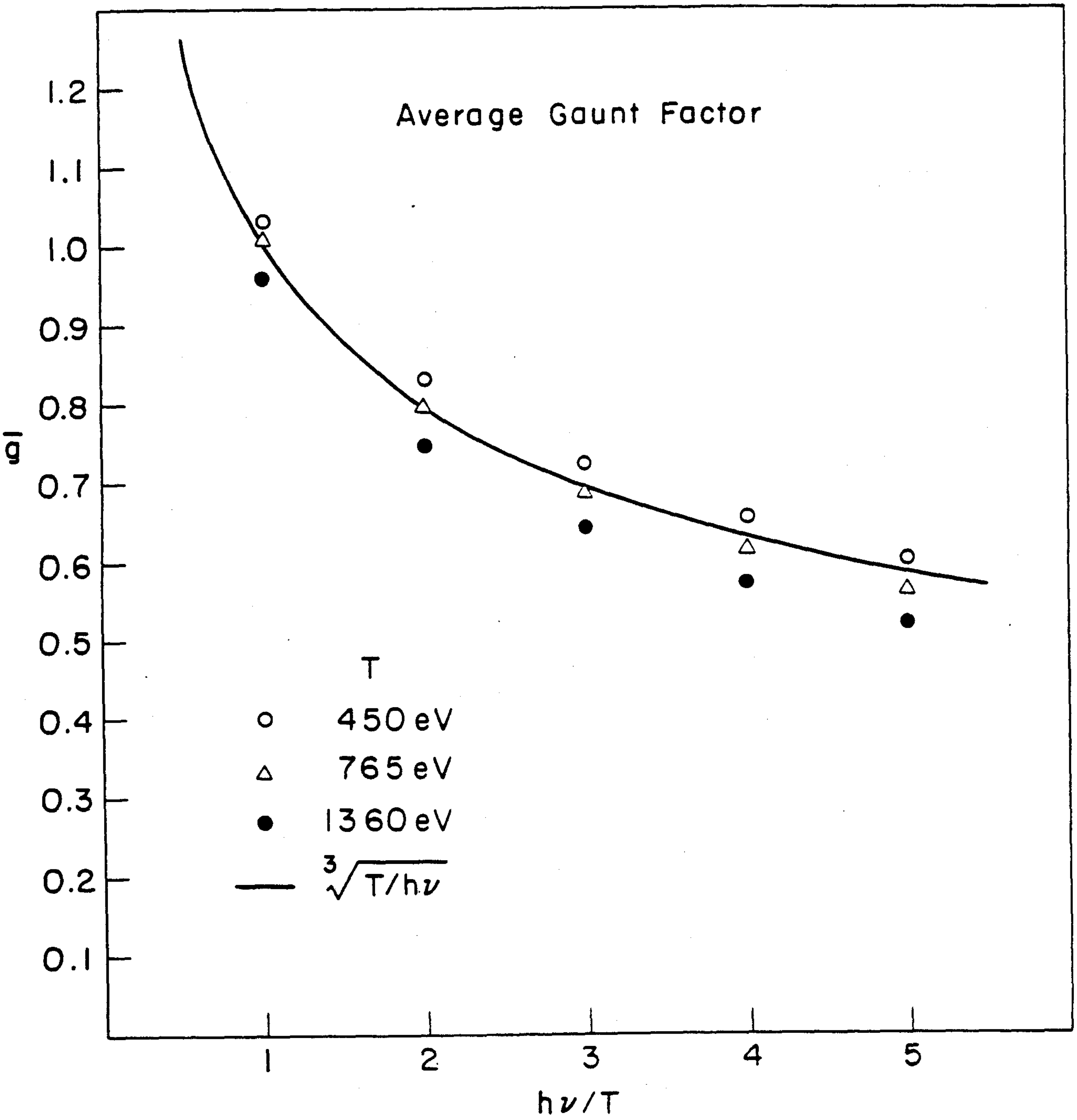

Average Gaunt Factor
$\bar{g}$
1.2
1.1
1.0
0.9
0.8
0.7
0.6
0.5
0.4
0.3
0.2
0.1
1
2
3
4
5
$h\nu/T$
T
○ 450 eV
△ 765 eV
● 1360 eV
$\sqrt[3]{T/h\nu}$

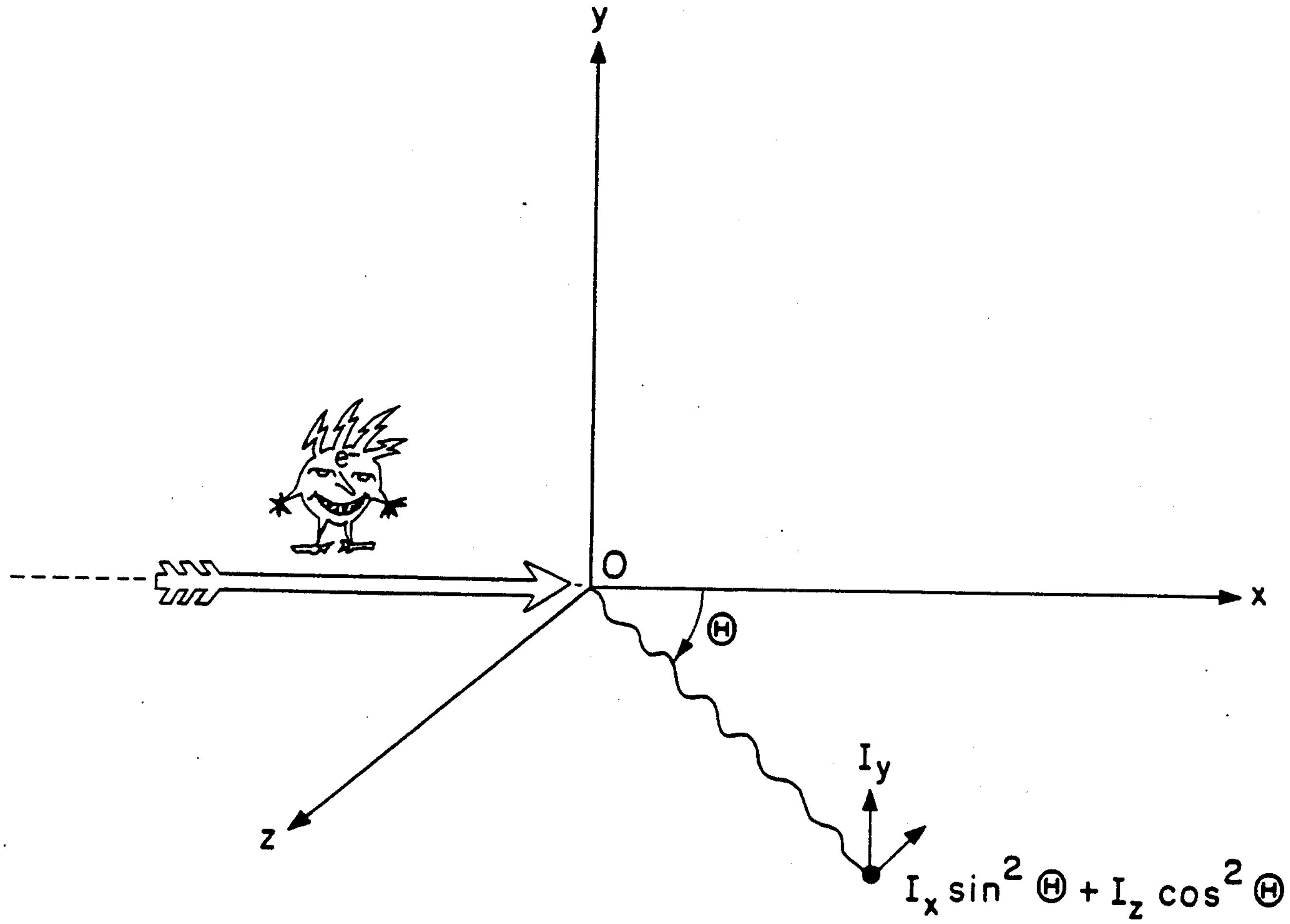

Collision Geometry

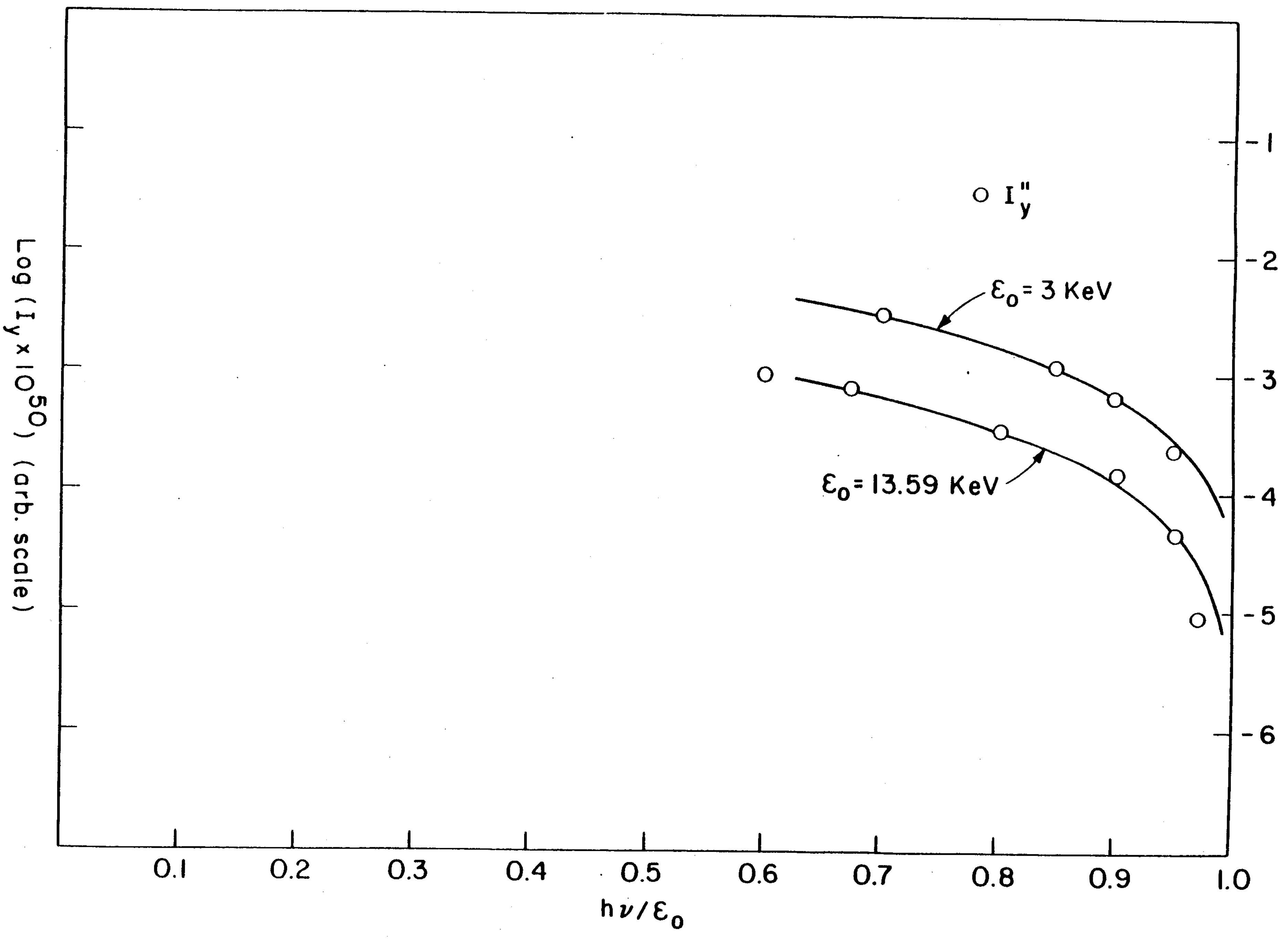

-1
-2
-3
-4
-5
-6
○ I''_y
$\mathcal{E}_0$ = 3 KeV
$\mathcal{E}_0$ = 13.59 KeV
0.1
0.2
0.3
0.4
0.5
0.6
0.7
0.8
0.9
1.0
$h\nu/\mathcal{E}_0$
Log ($I_y \times 10^{50}$) (arb. scale)

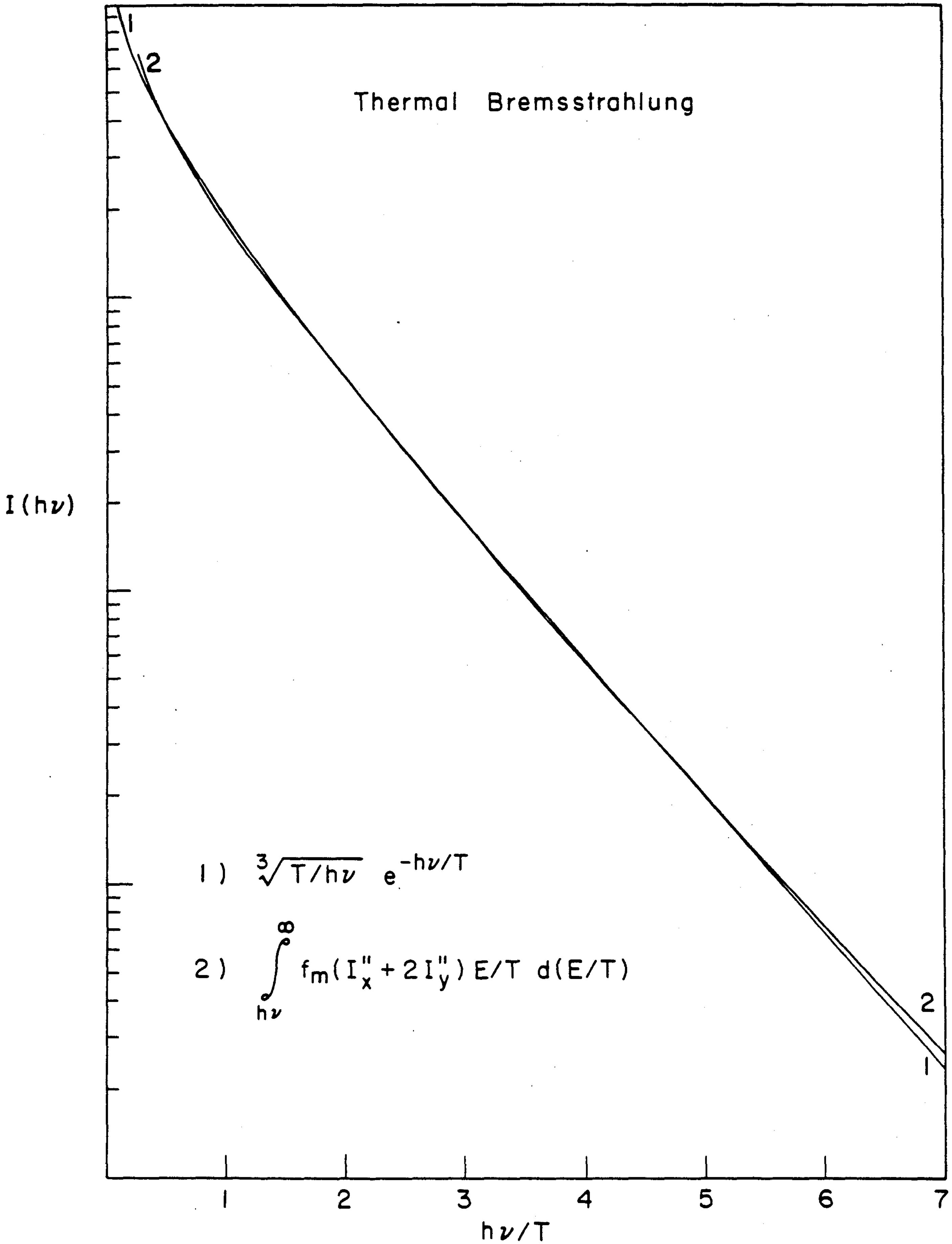
Thermal Bremsstrahlung
I(hν)
hν/T
1
2
3
4
5
6
7
1
2
1
2
1) $\sqrt[3]{T/h\nu}\; e^{-h\nu/T}$
2) $\int_{h\nu}^{\infty} f_m (I_x'' + 2I_y'')\, E/T \; d(E/T)$

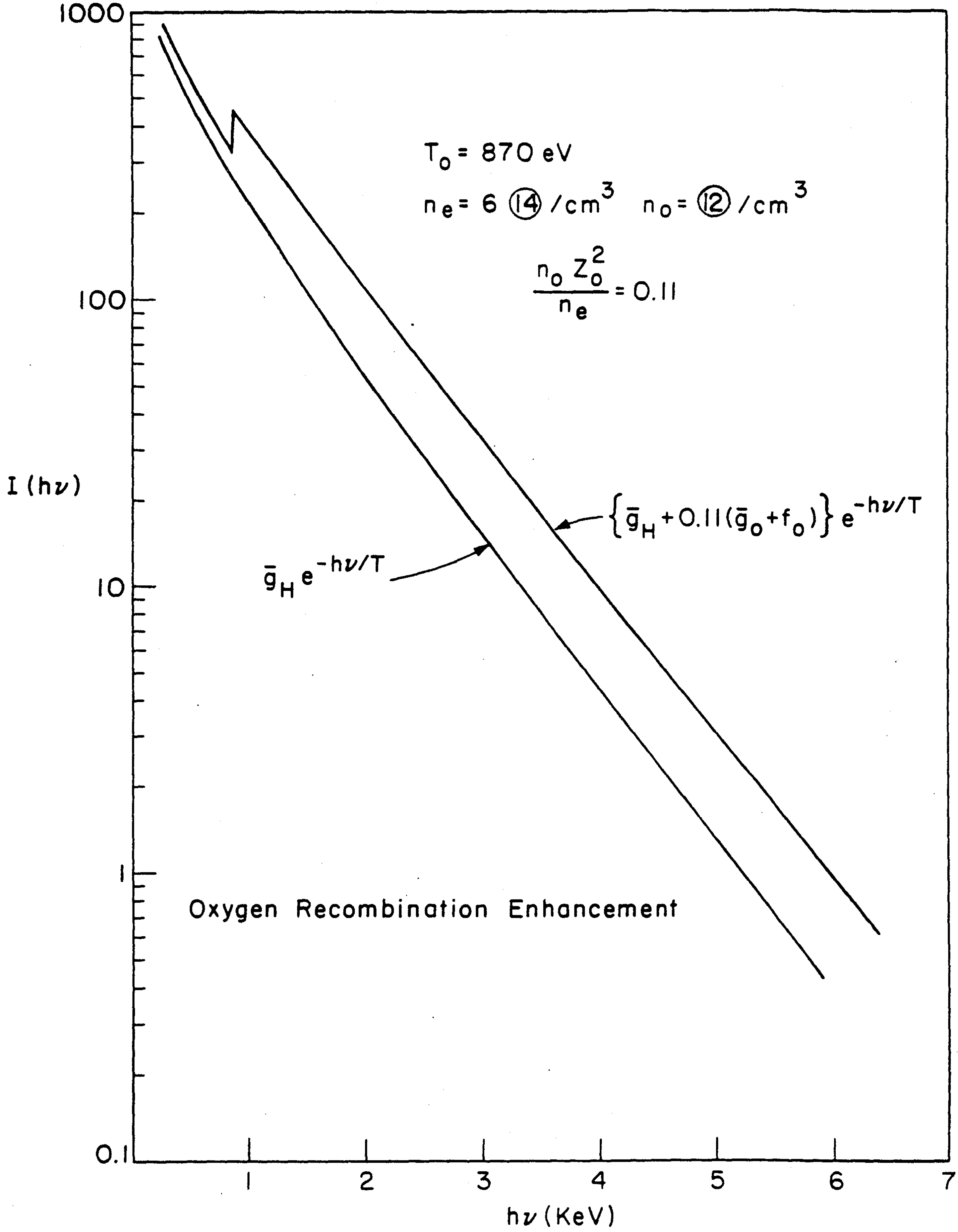
1000
100
10
1
0.1
I (hν)
1
2
3
4
5
6
7
hν (KeV)
T_o = 870 eV
n_e = 6 ⑭ /cm^3 n_o = ⑫ /cm^3
n_o Z_o^2 / n_e = 0.11
{ḡ_H + 0.11(ḡ_o + f_o)} e^{-hν/T}
ḡ_H e^{-hν/T}
Oxygen Recombination Enhancement

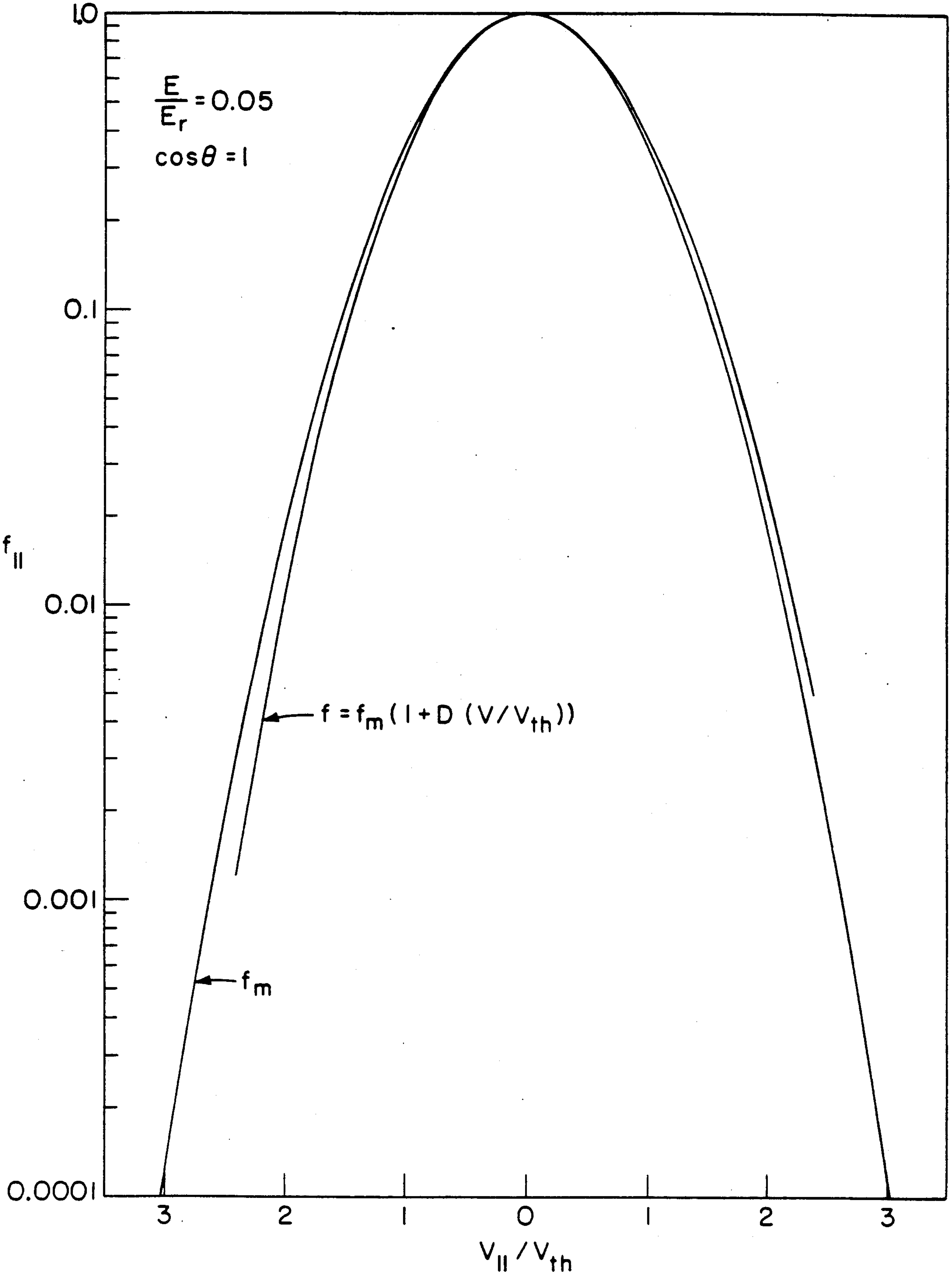
$\frac{E}{E_r} = 0.05$
$\cos\theta = 1$
$f = f_m(1 + D(V/V_{th}))$
f_m
$f_{\parallel}$
1.0
0.1
0.01
0.001
0.0001
3
2
1
0
1
2
3
$V_{\parallel}/V_{th}$

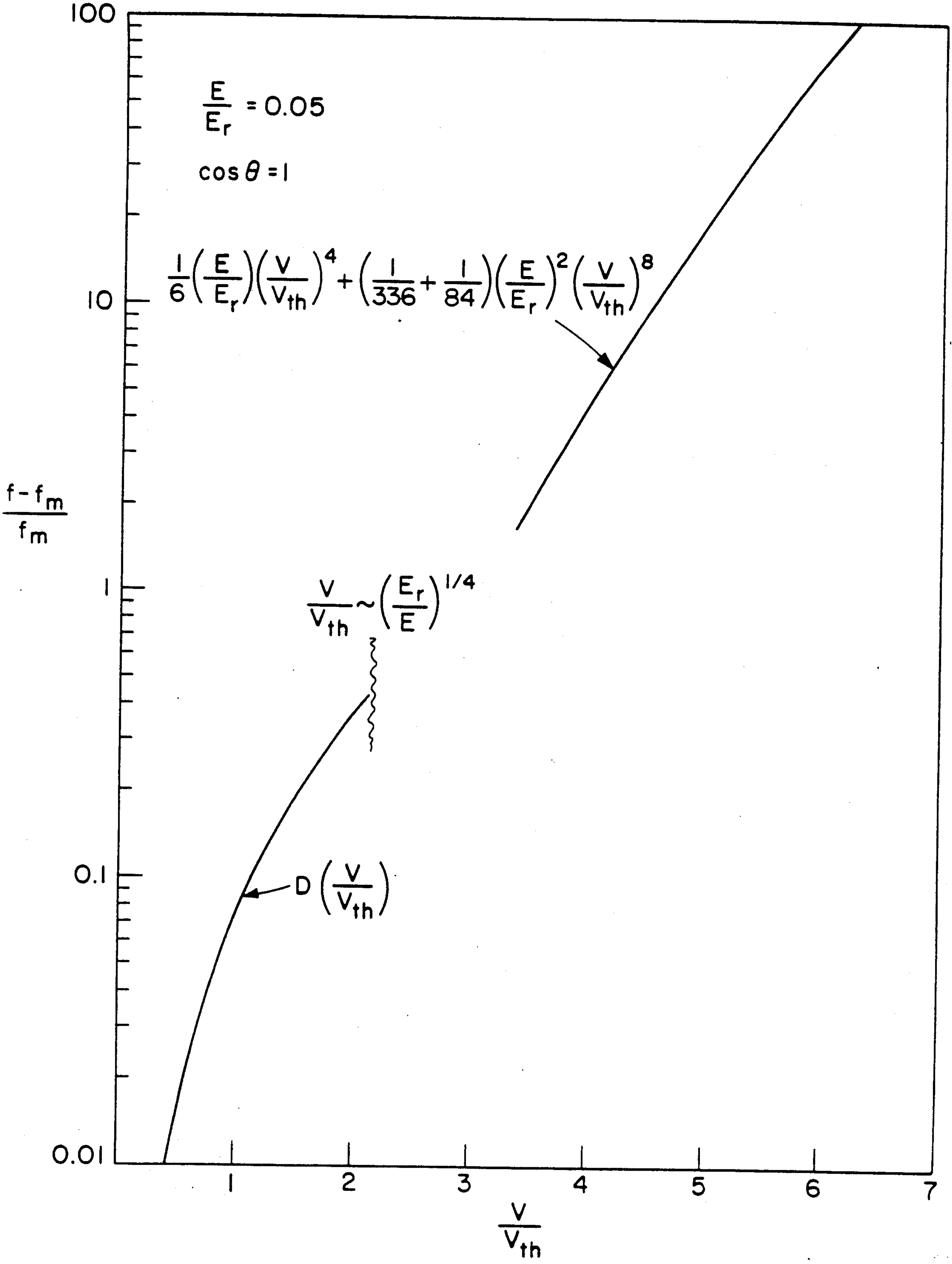
$\frac{E}{E_r} = 0.05$
$\cos\theta = 1$
$\frac{1}{6}\left(\frac{E}{E_r}\right)\left(\frac{V}{V_{th}}\right)^4 + \left(\frac{1}{336} + \frac{1}{84}\right)\left(\frac{E}{E_r}\right)^2\left(\frac{V}{V_{th}}\right)^8$
$\frac{V}{V_{th}} \sim \left(\frac{E_r}{E}\right)^{1/4}$
$D\left(\frac{V}{V_{th}}\right)$
$\frac{f - f_m}{f_m}$
100
10
1
0.1
0.01
1
2
3
4
5
6
7
$\frac{V}{V_{th}}$

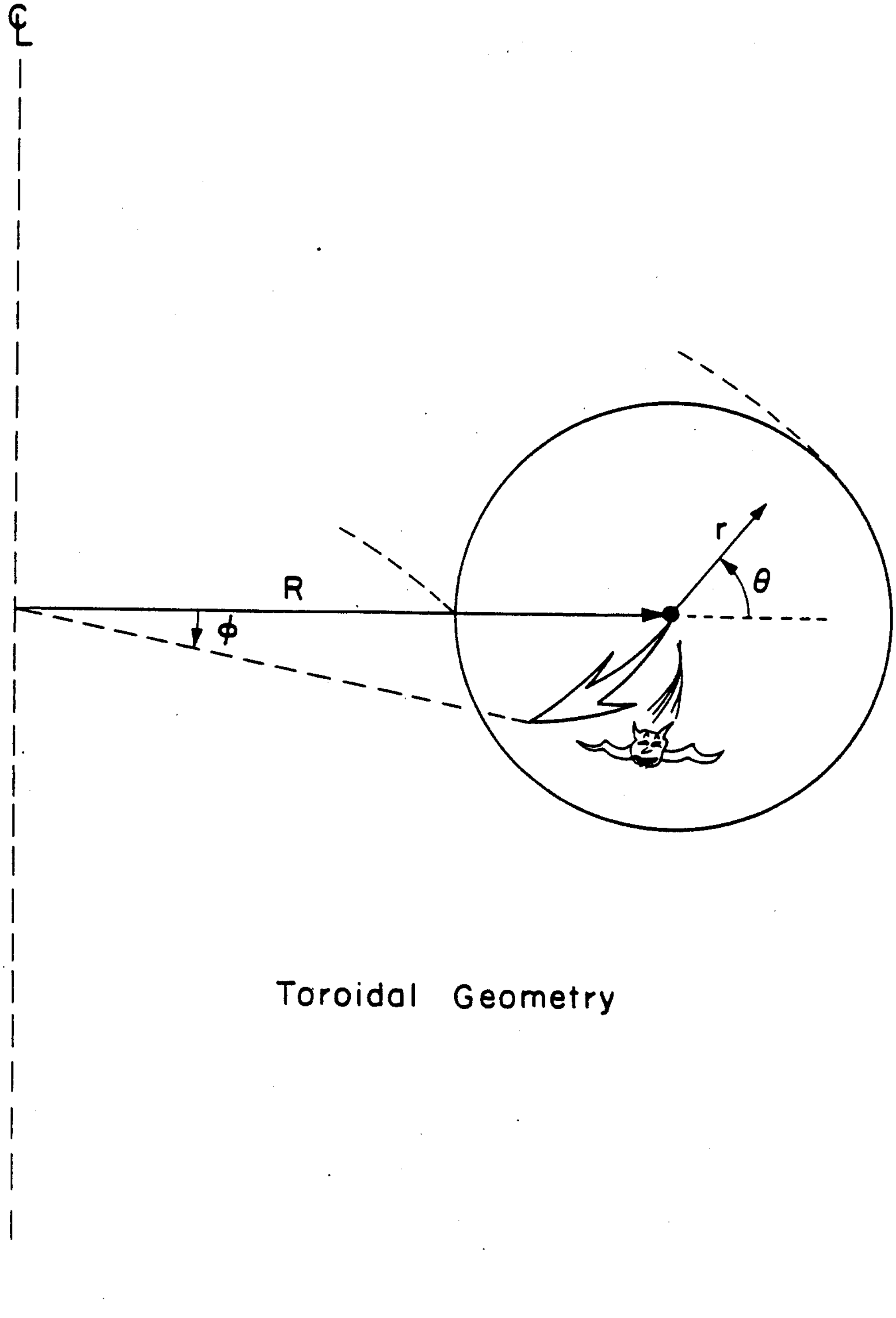

Toroidal Geometry

System Geometry

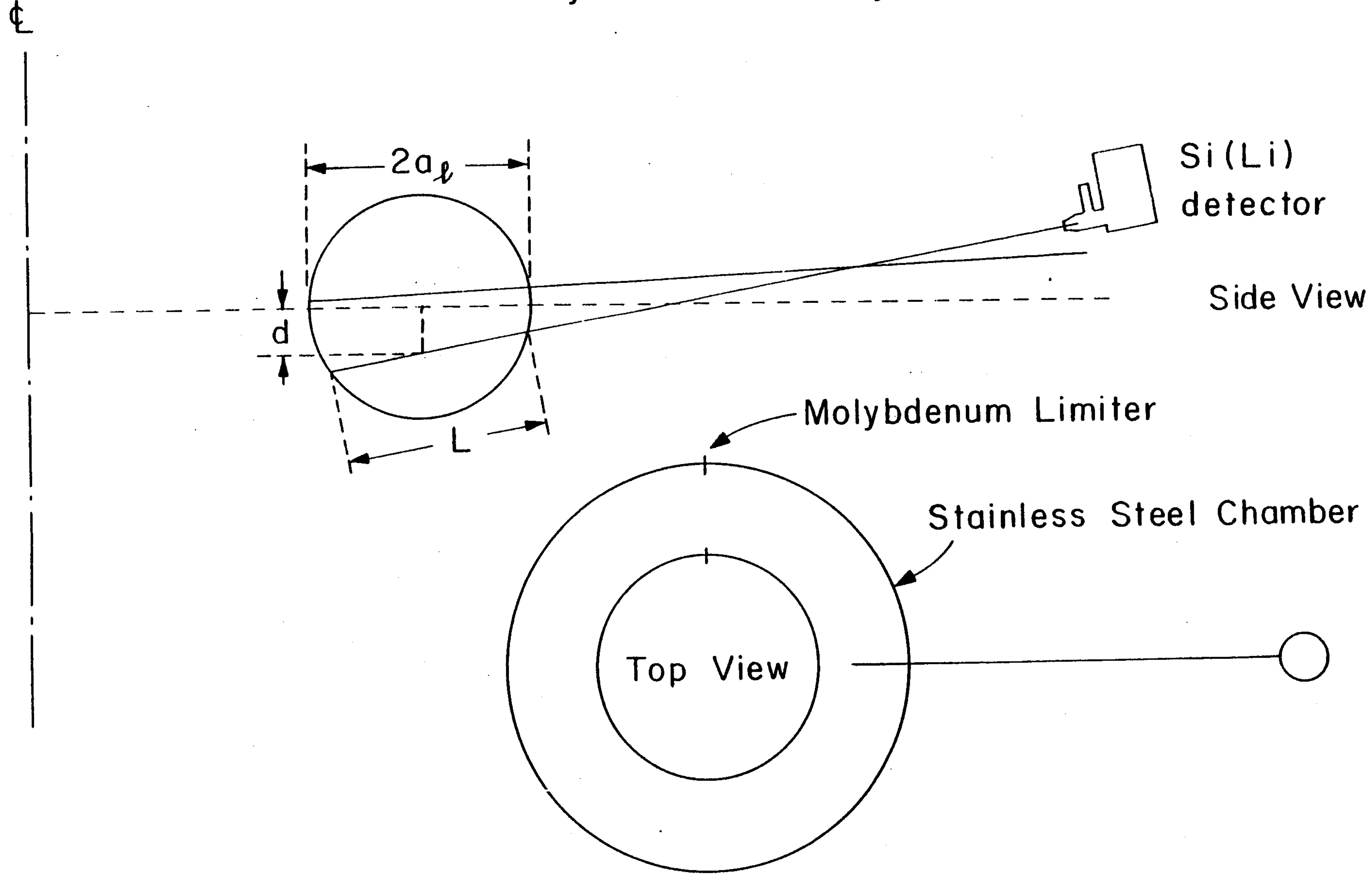

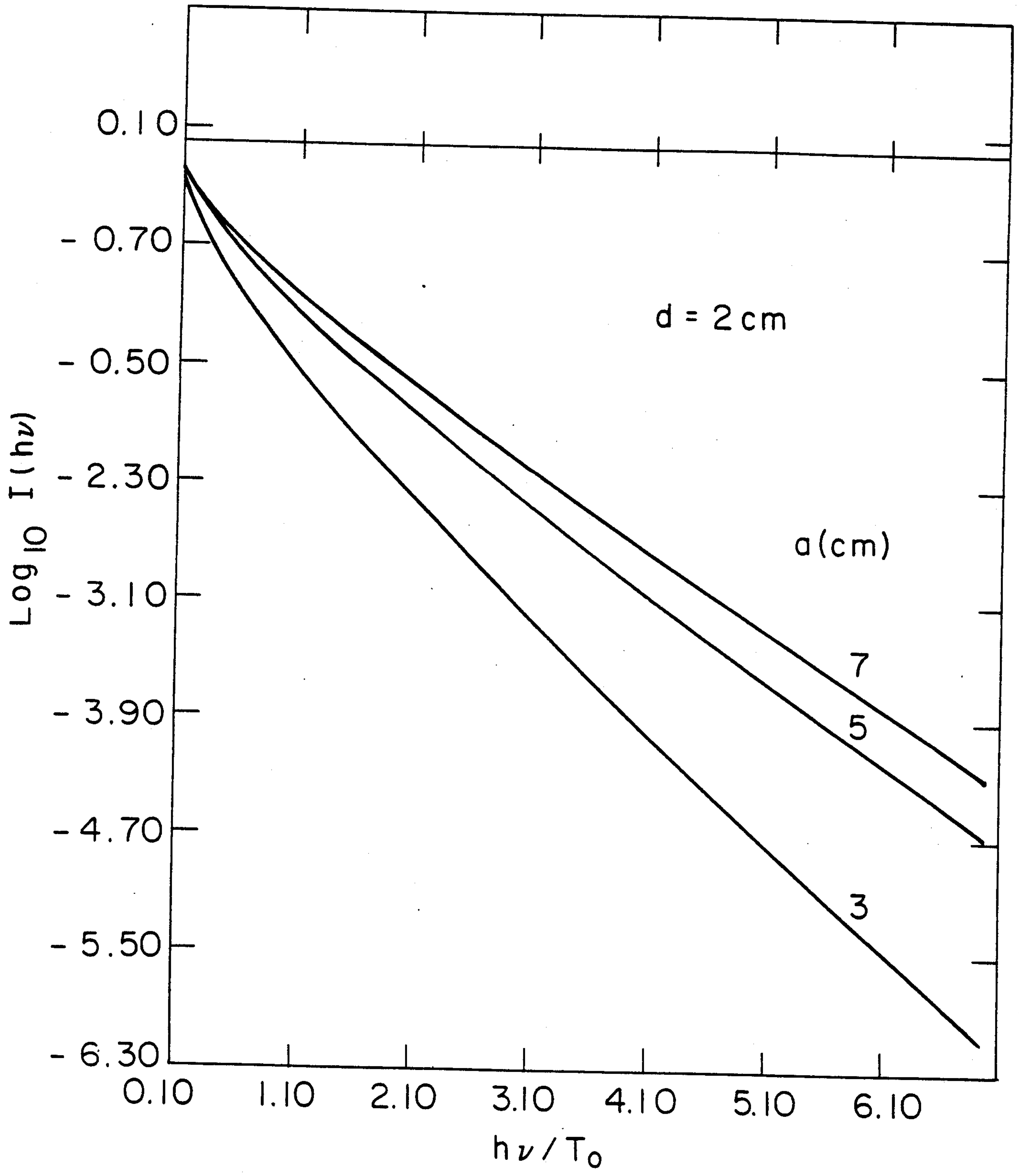

0.10
- 0.70
- 0.50
- 2.30
- 3.10
- 3.90
- 4.70
- 5.50
- 6.30
Log10 I(hν)
0.10
1.10
2.10
3.10
4.10
5.10
6.10
hν/T0
d = 2 cm
a(cm)
7
5
3

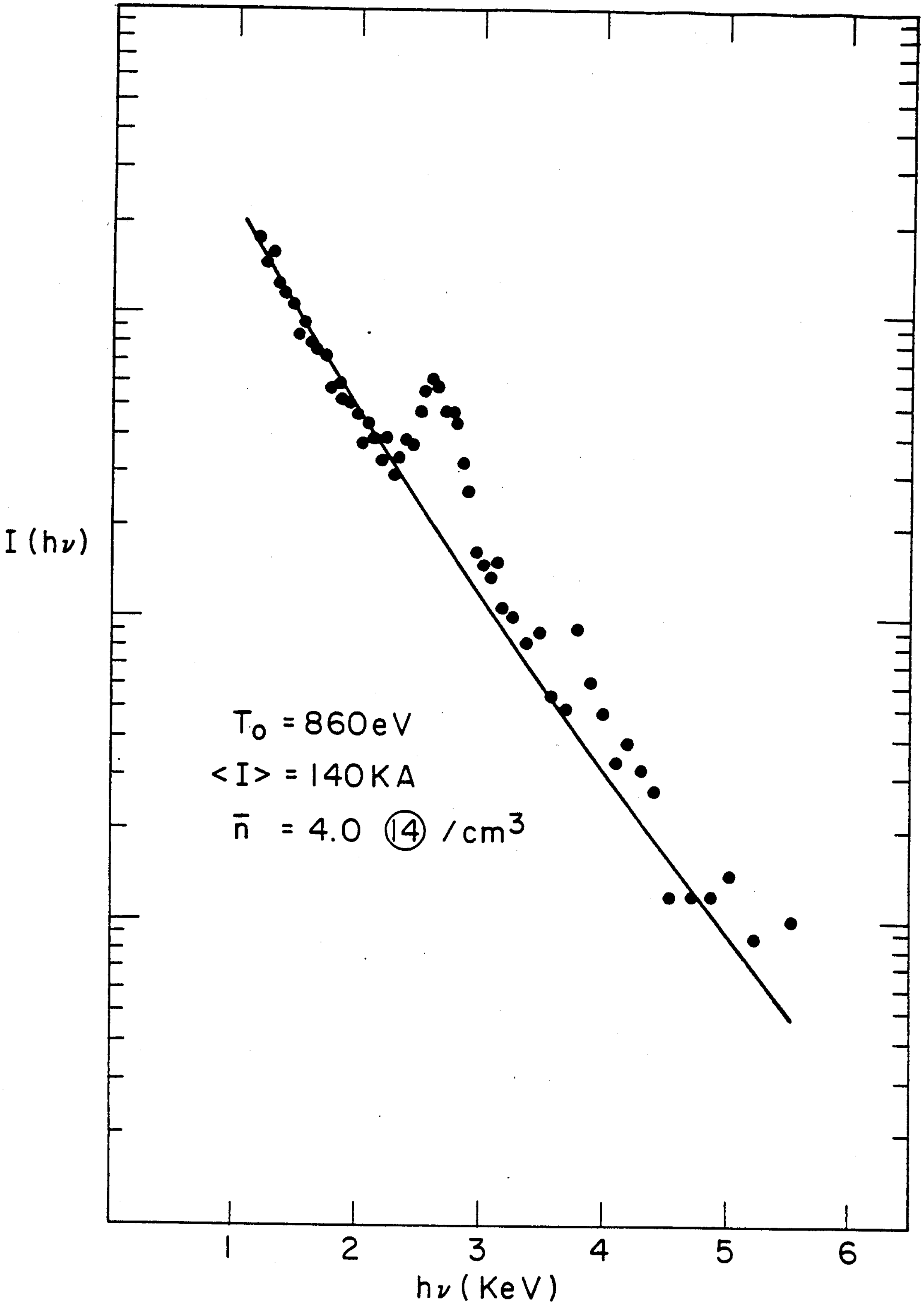
I (hν)
T_o = 860eV
<I> = 140KA
$\bar{n}$ = 4.0 ⑭ /cm^3
1
2
3
4
5
6
hν (KeV)

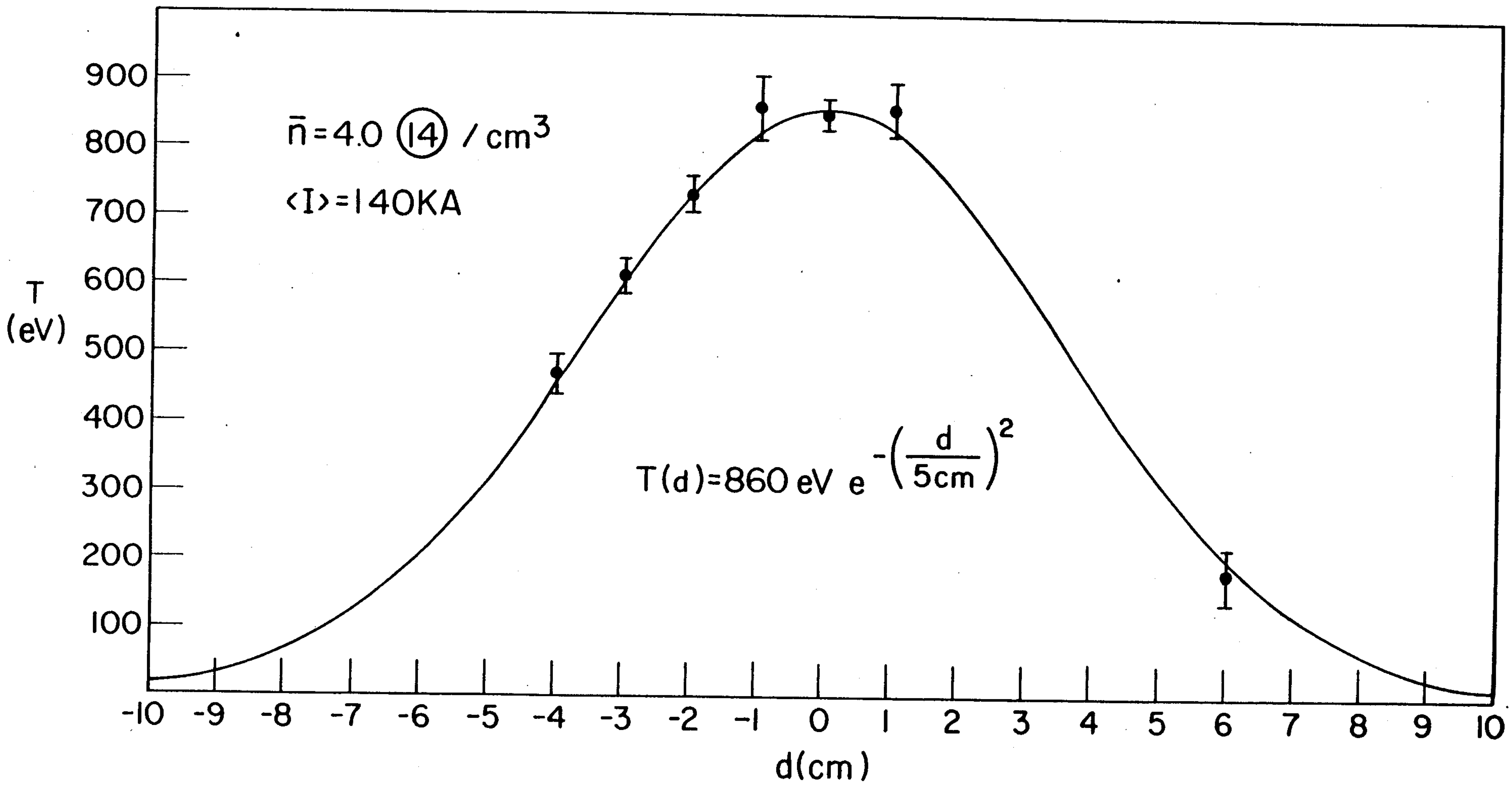
$\bar{n}$=4.0 ⑭ /cm^3
<I>=140KA
T(d)=860 eV $e^{-\left(\frac{d}{5cm}\right)^2}$
T
(eV)
900
800
700
600
500
400
300
200
100
-10
-9
-8
-7
-6
-5
-4
-3
-2
-1
0
1
2
3
4
5
6
7
8
9
10
d(cm)

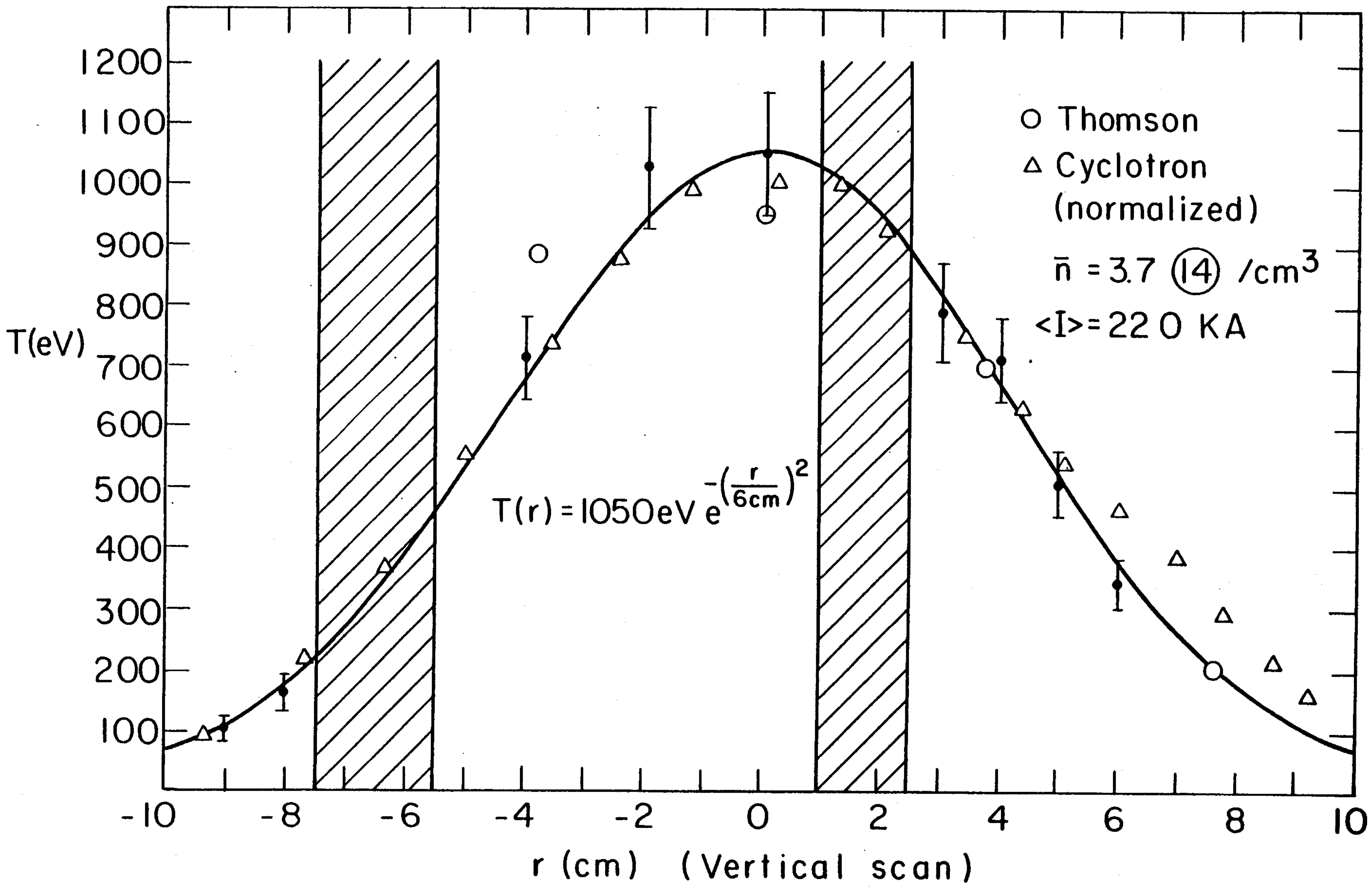
1200
1100
1000
900
800
700
600
500
400
300
200
100
T(eV)
-10
-8
-6
-4
-2
0
2
4
6
8
10
r (cm) (Vertical scan)
○ Thomson
△ Cyclotron (normalized)
$\bar{n} = 3.7$ ⑭ $/\text{cm}^3$
<I>=220 KA
$T(r) = 1050\,\text{eV}\, e^{-\left(\frac{r}{6\text{cm}}\right)^2}$

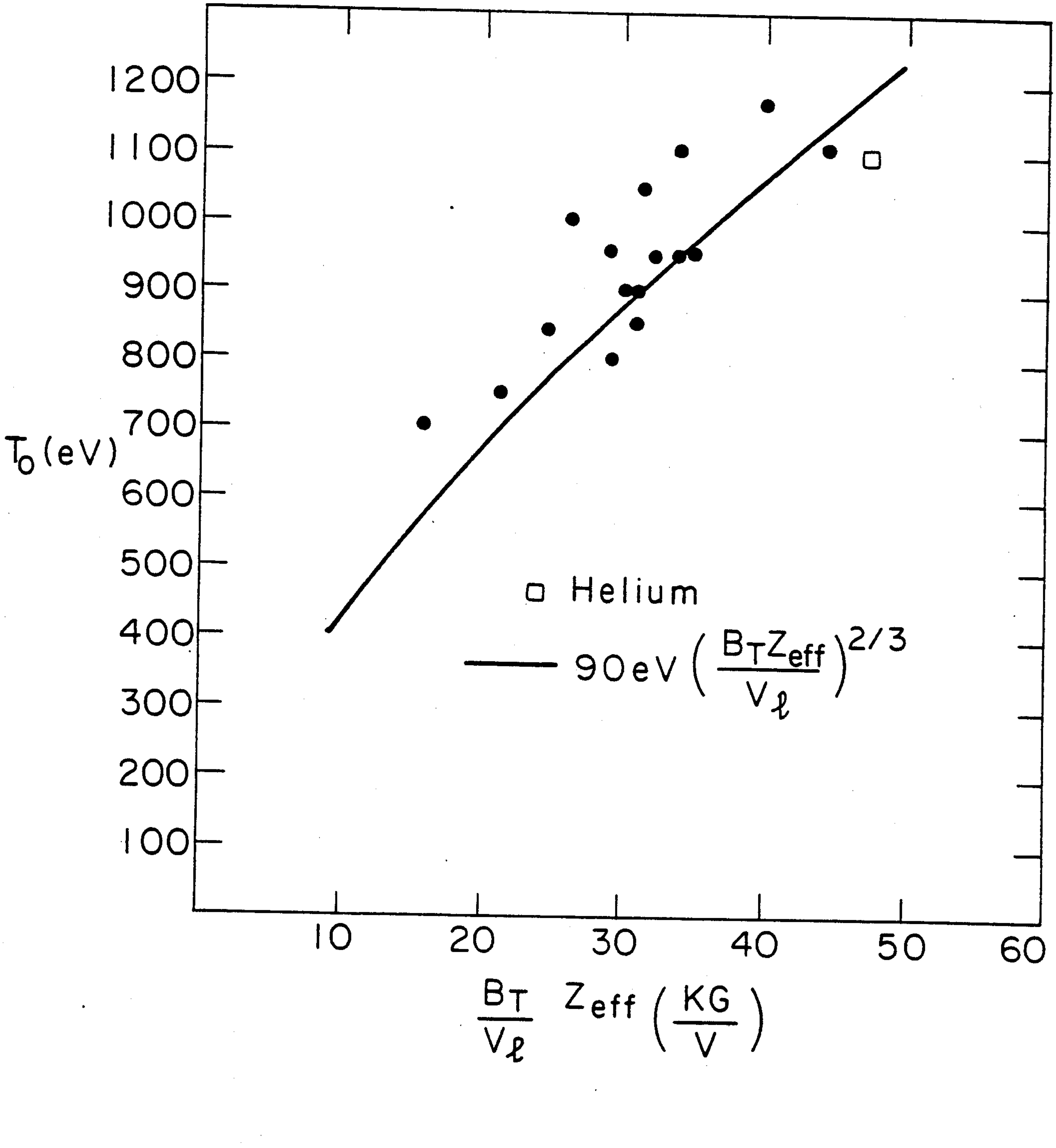

1200
1100
1000
900
800
700
600
500
400
300
200
100
T_0 (eV)
10
20
30
40
50
60
$\frac{B_T}{V_\ell}$ Z_{eff} $\left(\frac{KG}{V}\right)$
□ Helium
$90\,eV\left(\frac{B_T Z_{eff}}{V_\ell}\right)^{2/3}$

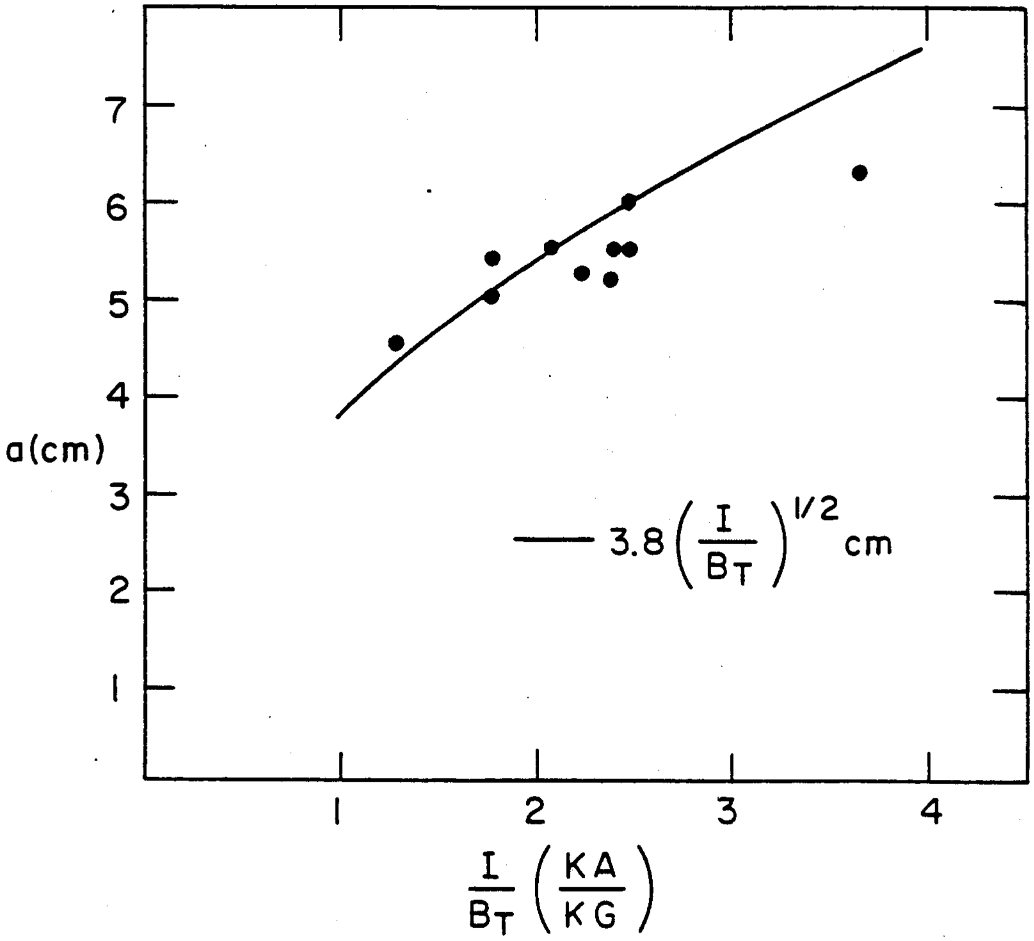

a(cm)
1
2
3
4
5
6
7
1
2
3
4
$\frac{I}{B_T}\left(\frac{KA}{KG}\right)$
$3.8\left(\frac{I}{B_T}\right)^{1/2}$ cm

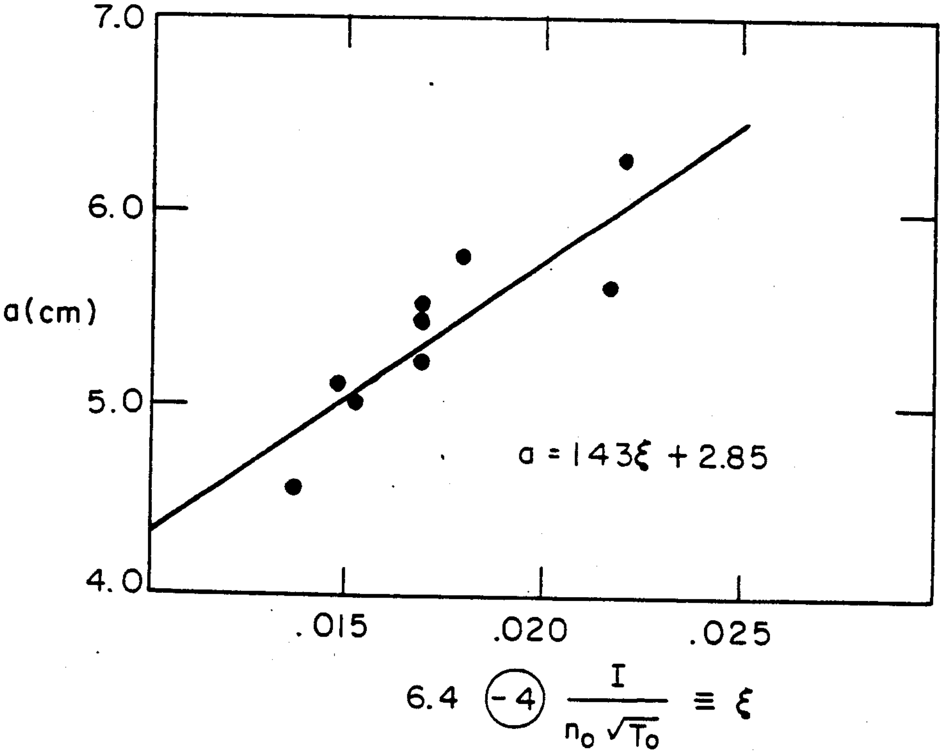
7.0
6.0
5.0
4.0
a(cm)
$a = 143\xi + 2.85$
.015
.020
.025
$6.4 \, \text{(-4)} \, \frac{I}{n_o \sqrt{T_o}} \equiv \xi$

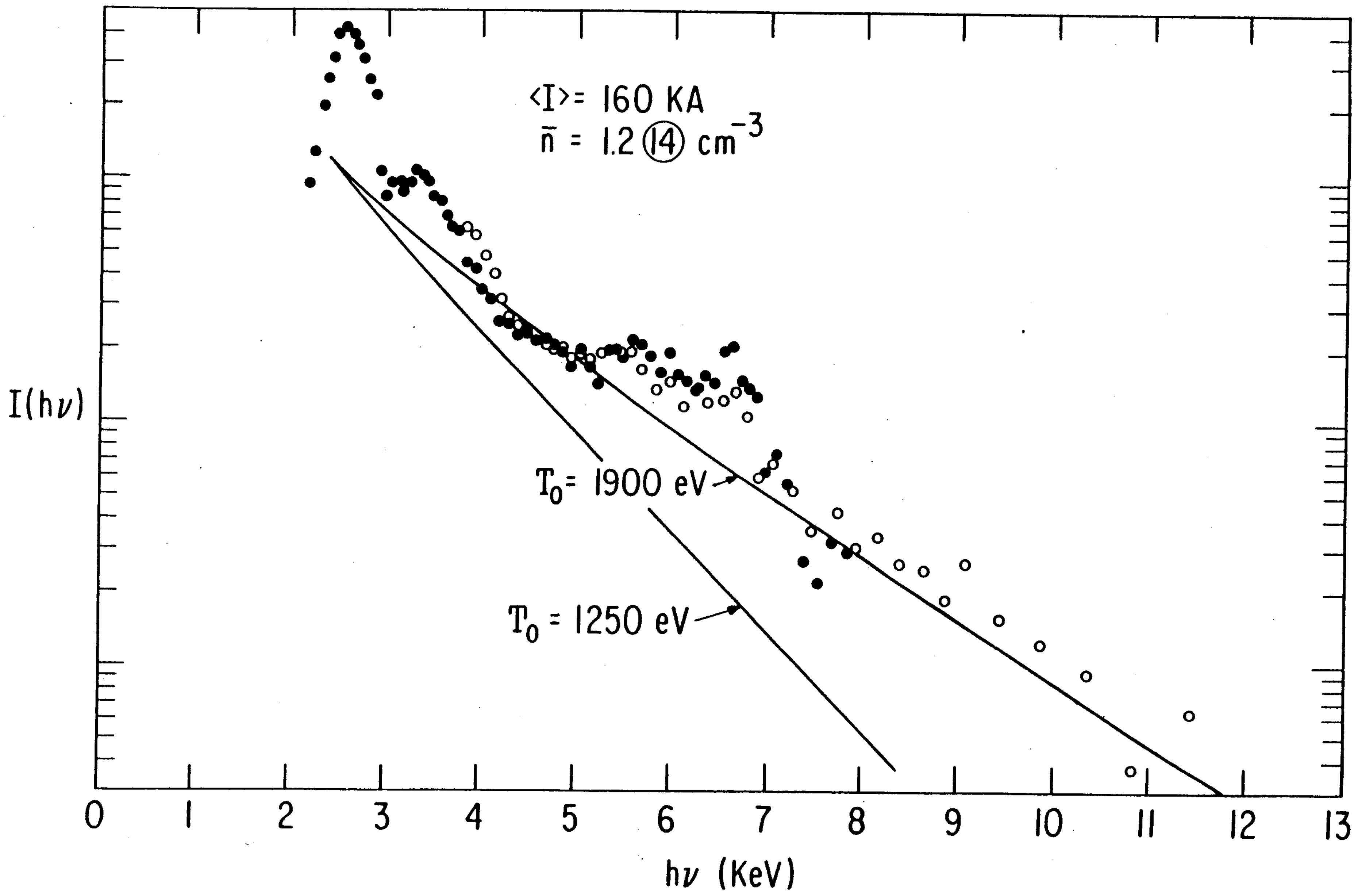

<I>= 160 KA
$\bar{n}$ = 1.2 ⑭ cm^{-3}
T_0= 1900 eV
T_0 = 1250 eV
I(hν)
0
1
2
3
4
5
6
7
8
9
10
11
12
13
hν (KeV)

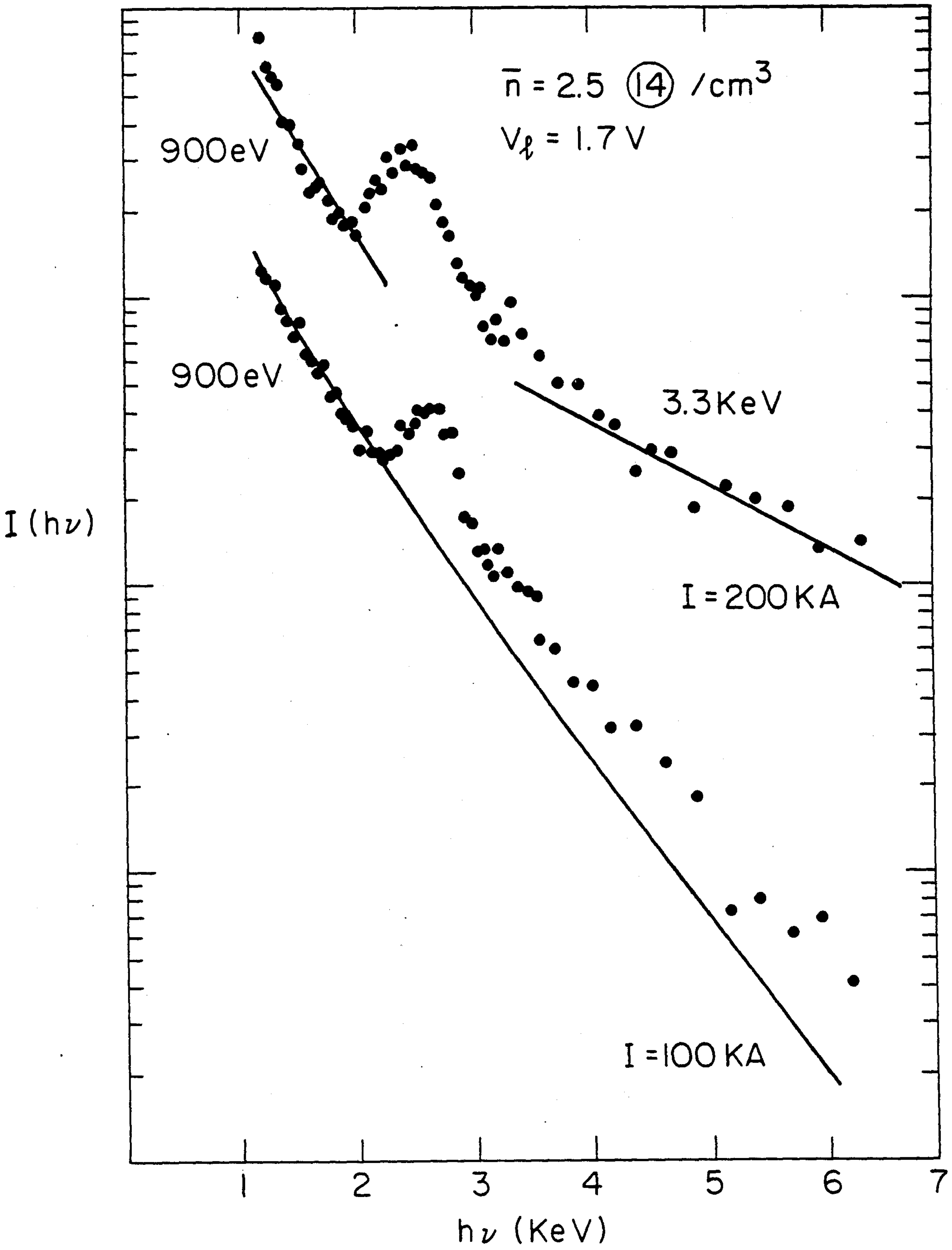
$\bar{n} = 2.5$ ⑭ $/cm^3$
$V_\ell = 1.7$ V
900eV
900eV
3.3KeV
I = 200 KA
I = 100 KA
I (hν)
1
2
3
4
5
6
7
hν (KeV)

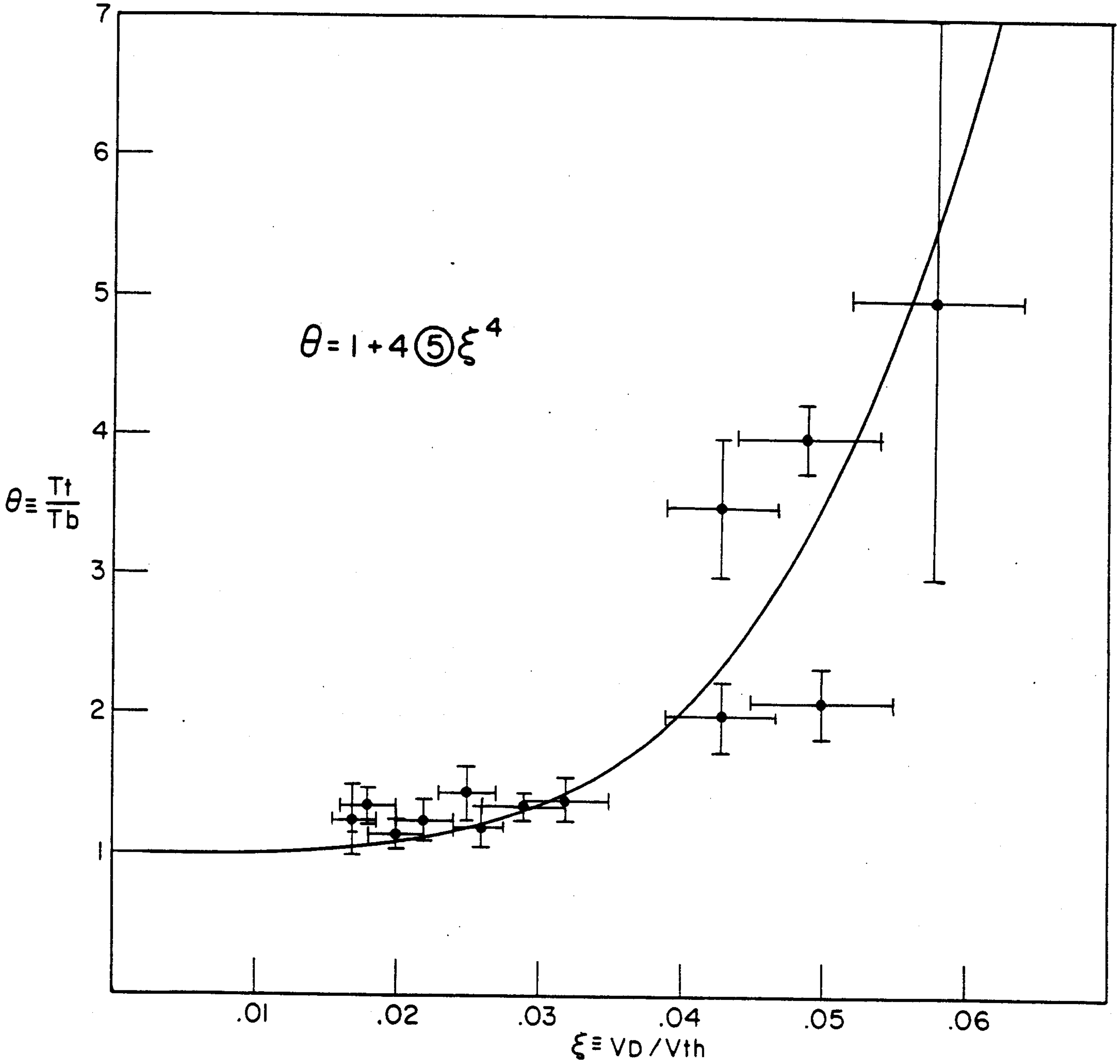
$\theta = 1 + 4⑤\xi^4$
$\theta \equiv \frac{Tt}{Tb}$
7
6
5
4
3
2
1
.01
.02
.03
.04
.05
.06
$\xi \equiv V_D / V_{th}$

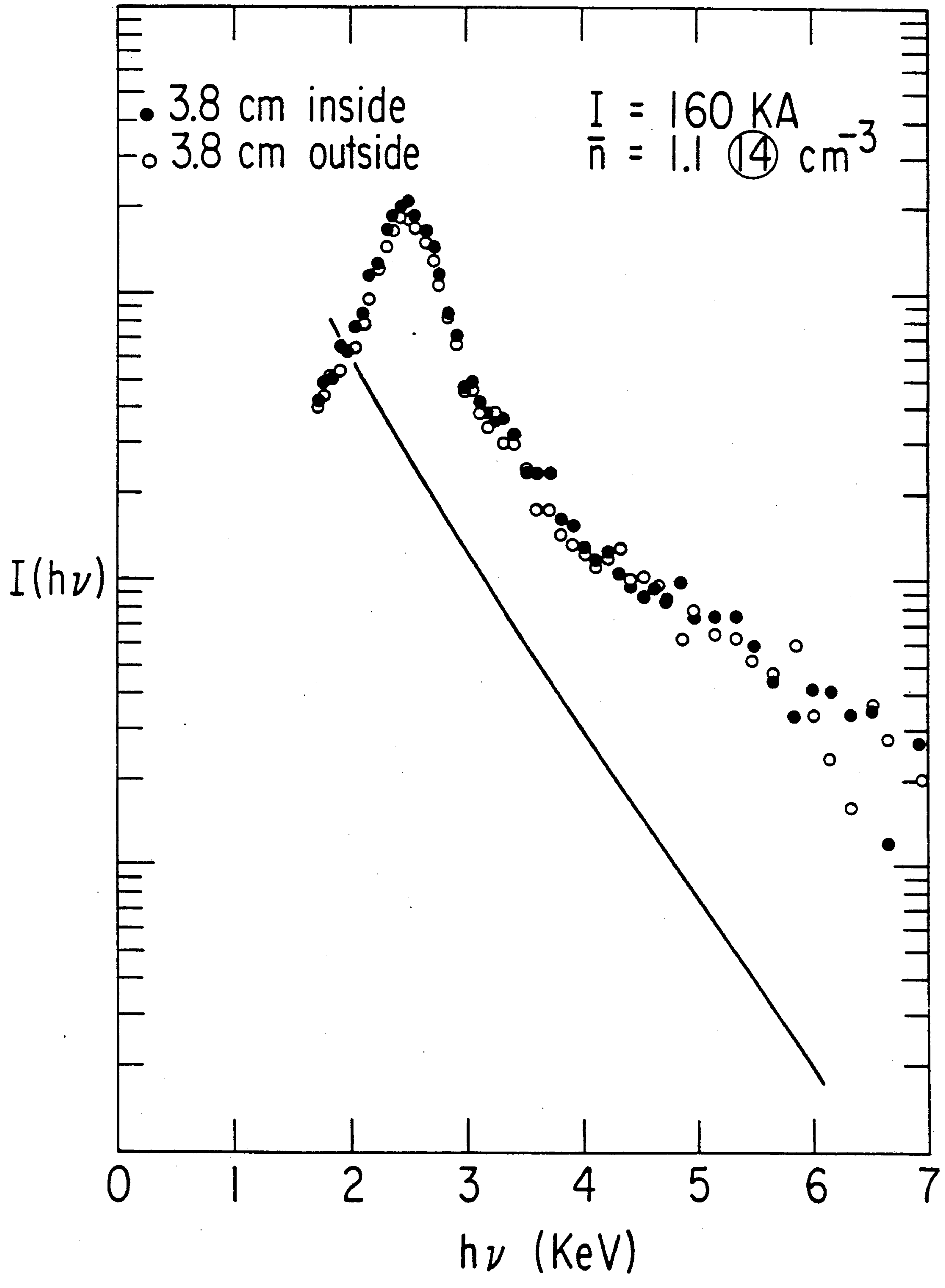
● 3.8 cm inside
○ 3.8 cm outside
I = 160 KA
n̄ = 1.1 ⑭ cm⁻³
I(hν)
0
1
2
3
4
5
6
7
hν (KeV)

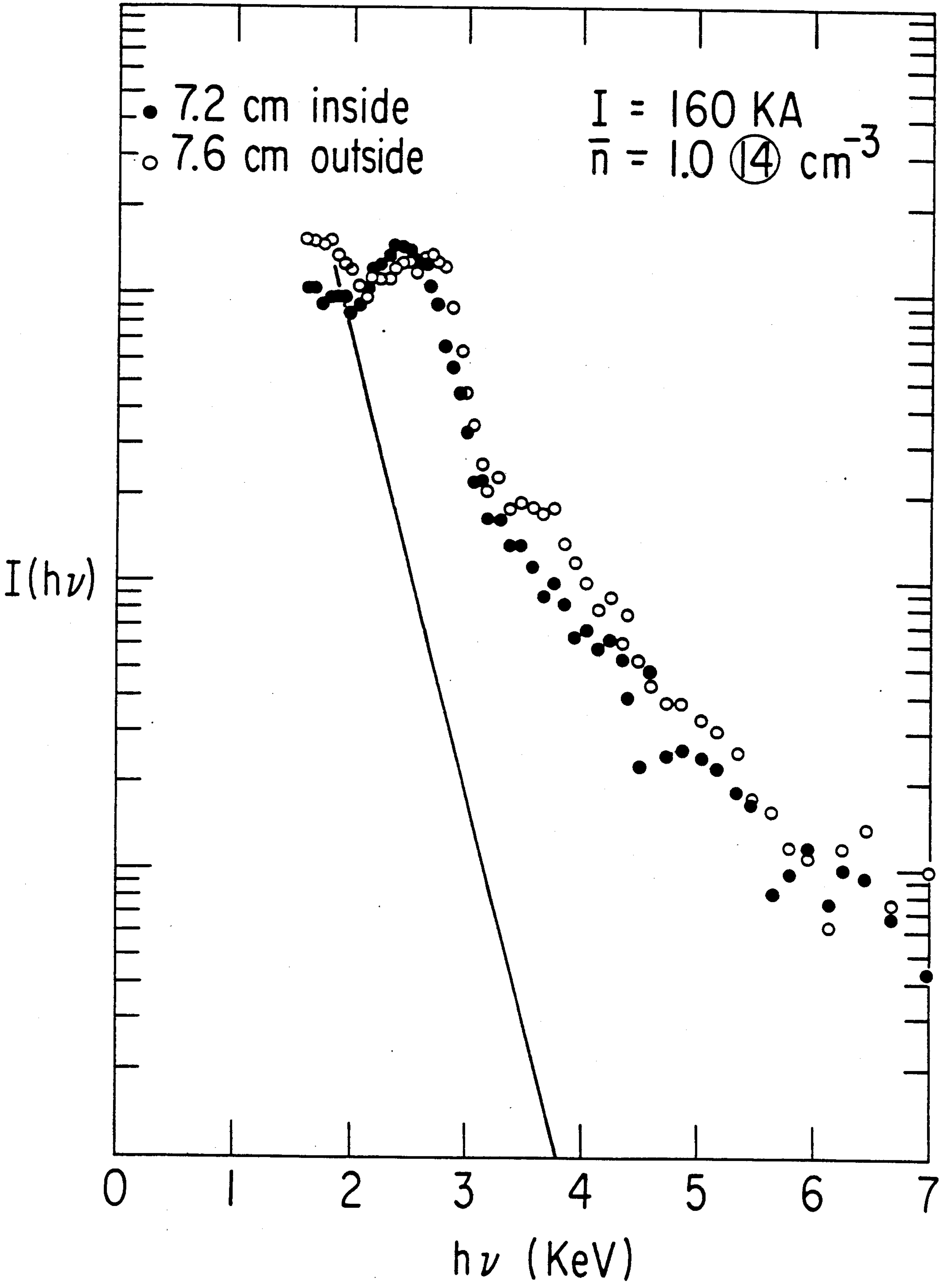

● 7.2 cm inside
○ 7.6 cm outside
I = 160 KA
n̄ = 1.0 ⑭ cm⁻³
I(hν)
0
1
2
3
4
5
6
7
hν (KeV)

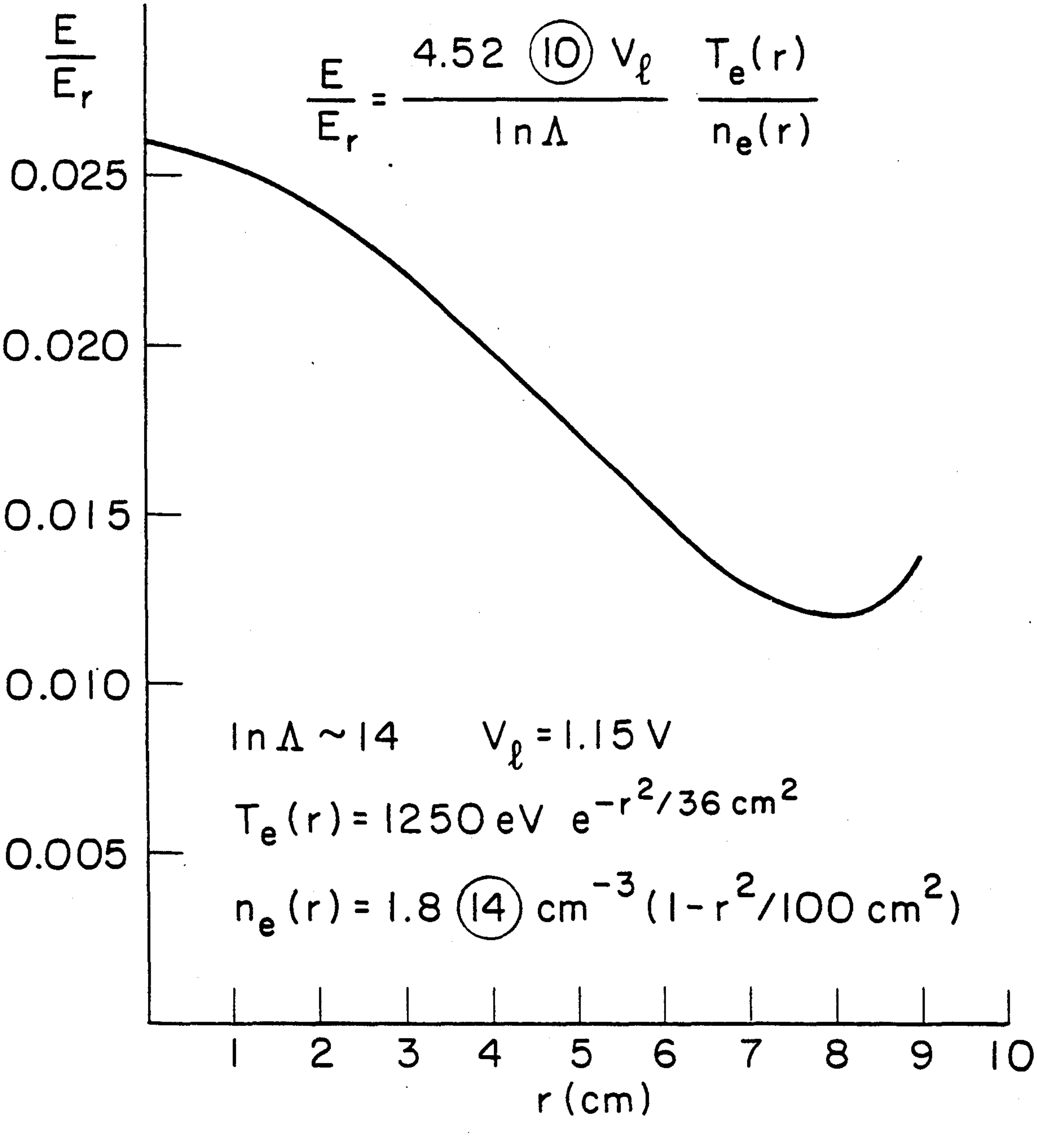
$\frac{E}{E_r}$
$\frac{E}{E_r} = \frac{4.52 \text{ ⑩ } V_\ell}{\ln \Lambda} \frac{T_e(r)}{n_e(r)}$
0.025
0.020
0.015
0.010
0.005
$\ln \Lambda \sim 14$ $V_\ell = 1.15$ V
$T_e(r) = 1250$ eV $e^{-r^2/36 \text{ cm}^2}$
$n_e(r) = 1.8$ ⑭ $\text{cm}^{-3} (1 - r^2/100 \text{ cm}^2)$
1
2
3
4
5
6
7
8
9
10
r (cm)

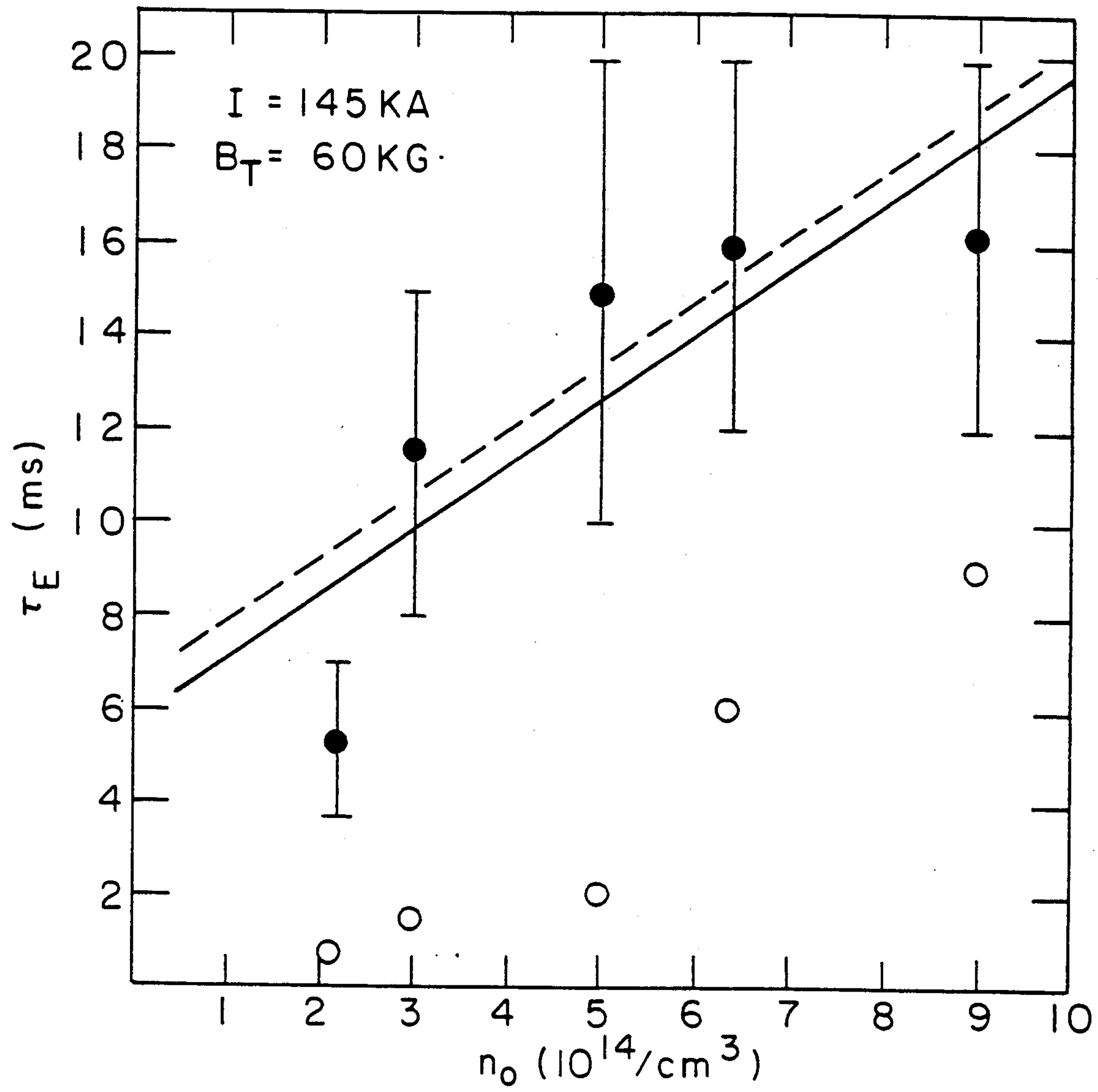
I = 145 KA
B_T = 60 KG
τ_E (ms)
20
18
16
14
12
10
8
6
4
2
1
2
3
4
5
6
7
8
9
10
n_0 (10^{14}/cm^3)

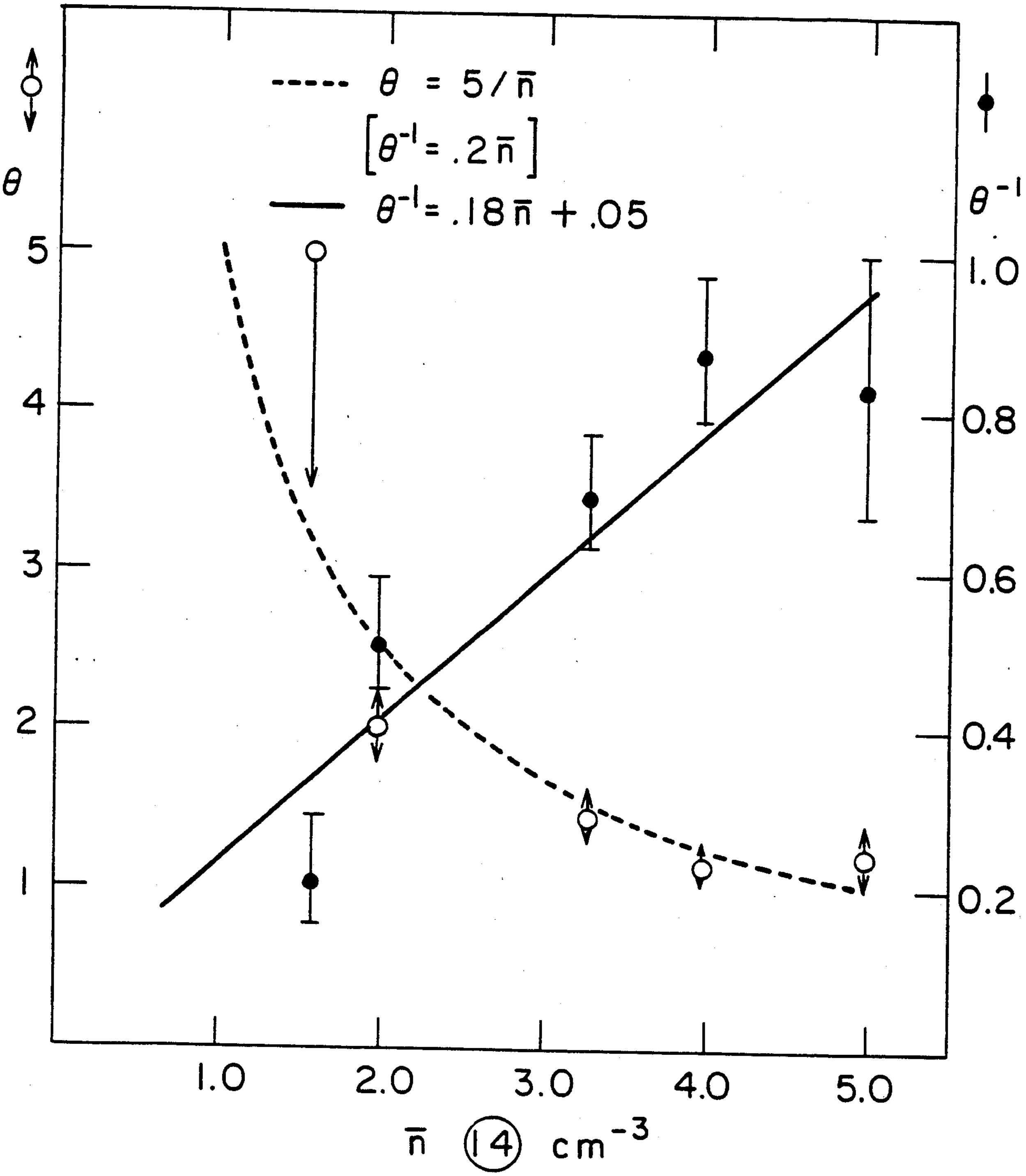
θ = 5/n̄
[θ⁻¹ = .2 n̄]
θ⁻¹ = .18 n̄ + .05
θ
θ⁻¹
5
4
3
2
1
1.0
0.8
0.6
0.4
0.2
1.0
2.0
3.0
4.0
5.0
n̄ ⑭ cm⁻³

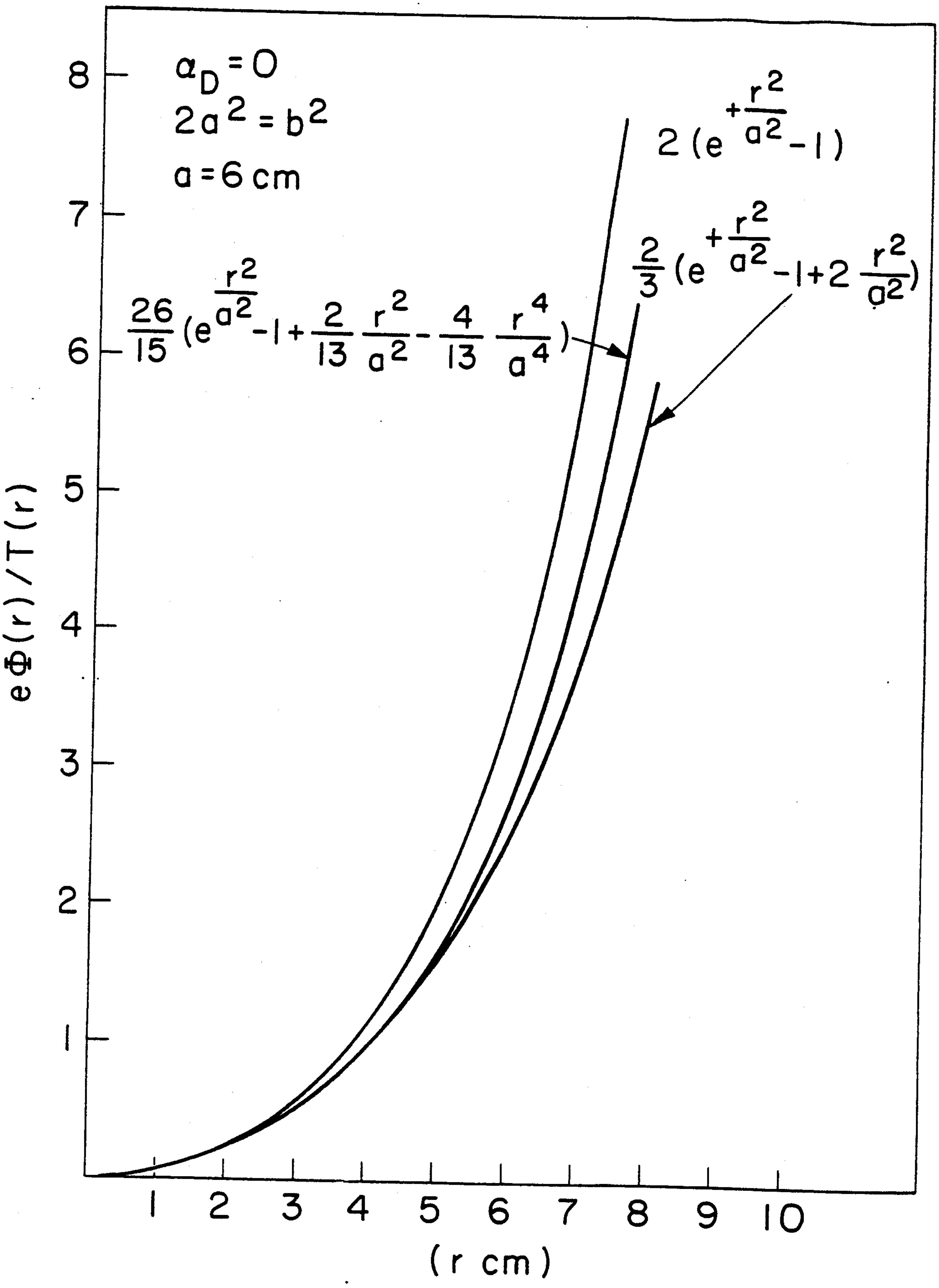
$\alpha_D = 0$
$2a^2 = b^2$
$a = 6$ cm
$2\,(e^{+\frac{r^2}{a^2}} - 1)$
$\frac{2}{3}\,(e^{+\frac{r^2}{a^2}} - 1 + 2\,\frac{r^2}{a^2})$
$\frac{26}{15}\,(e^{\frac{r^2}{a^2}} - 1 + \frac{2}{13}\,\frac{r^2}{a^2} - \frac{4}{13}\,\frac{r^4}{a^4})$
$e\Phi(r)/T(r)$
1
2
3
4
5
6
7
8
9
10
(r cm)

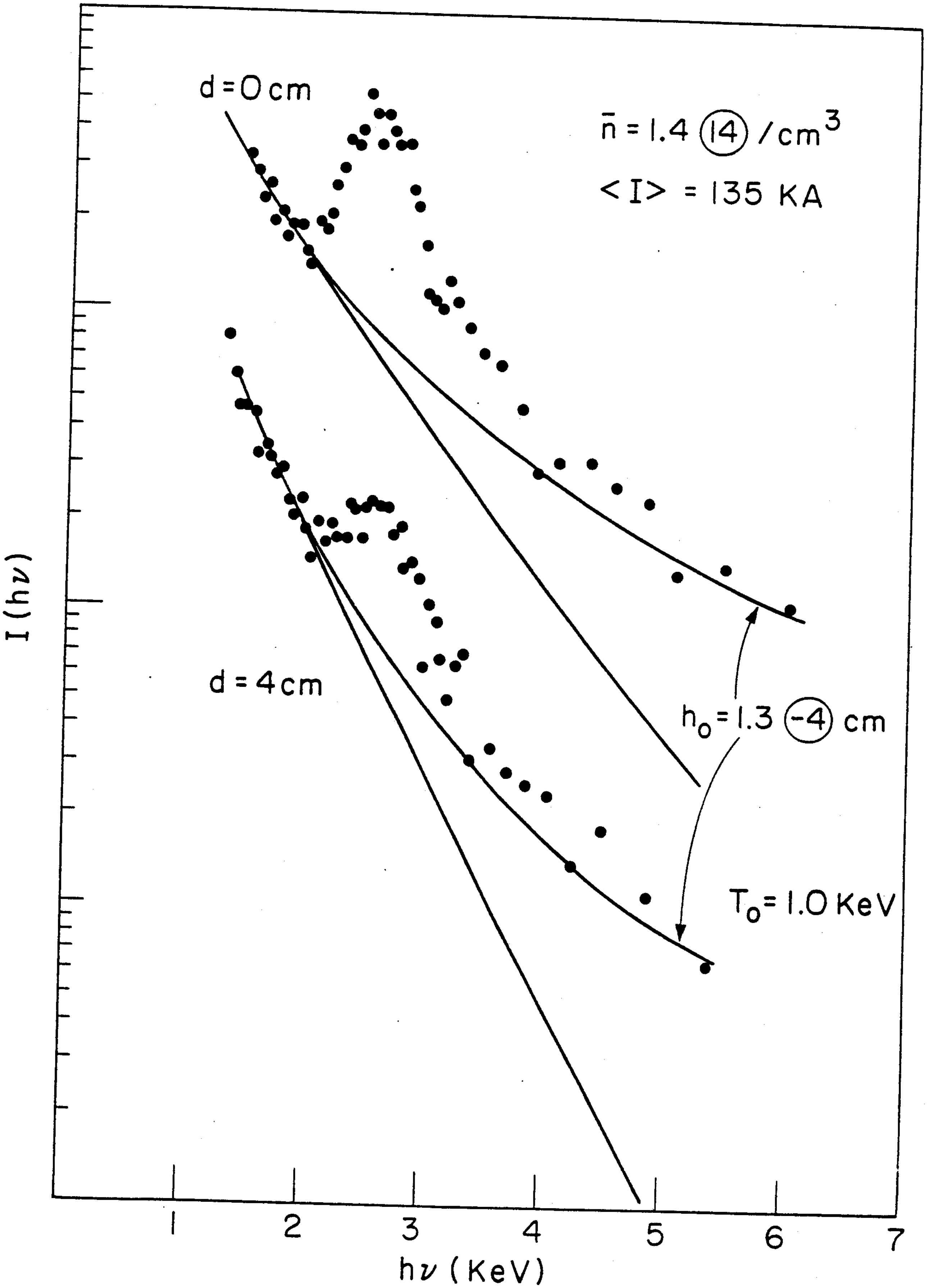

d = 0 cm
$\bar{n} = 1.4 (14) /cm^3$
<I> = 135 KA
d = 4 cm
$h_0 = 1.3 (-4)$ cm
$T_0 = 1.0$ KeV
I (hν)
hν (KeV)
1
2
3
4
5
6
7

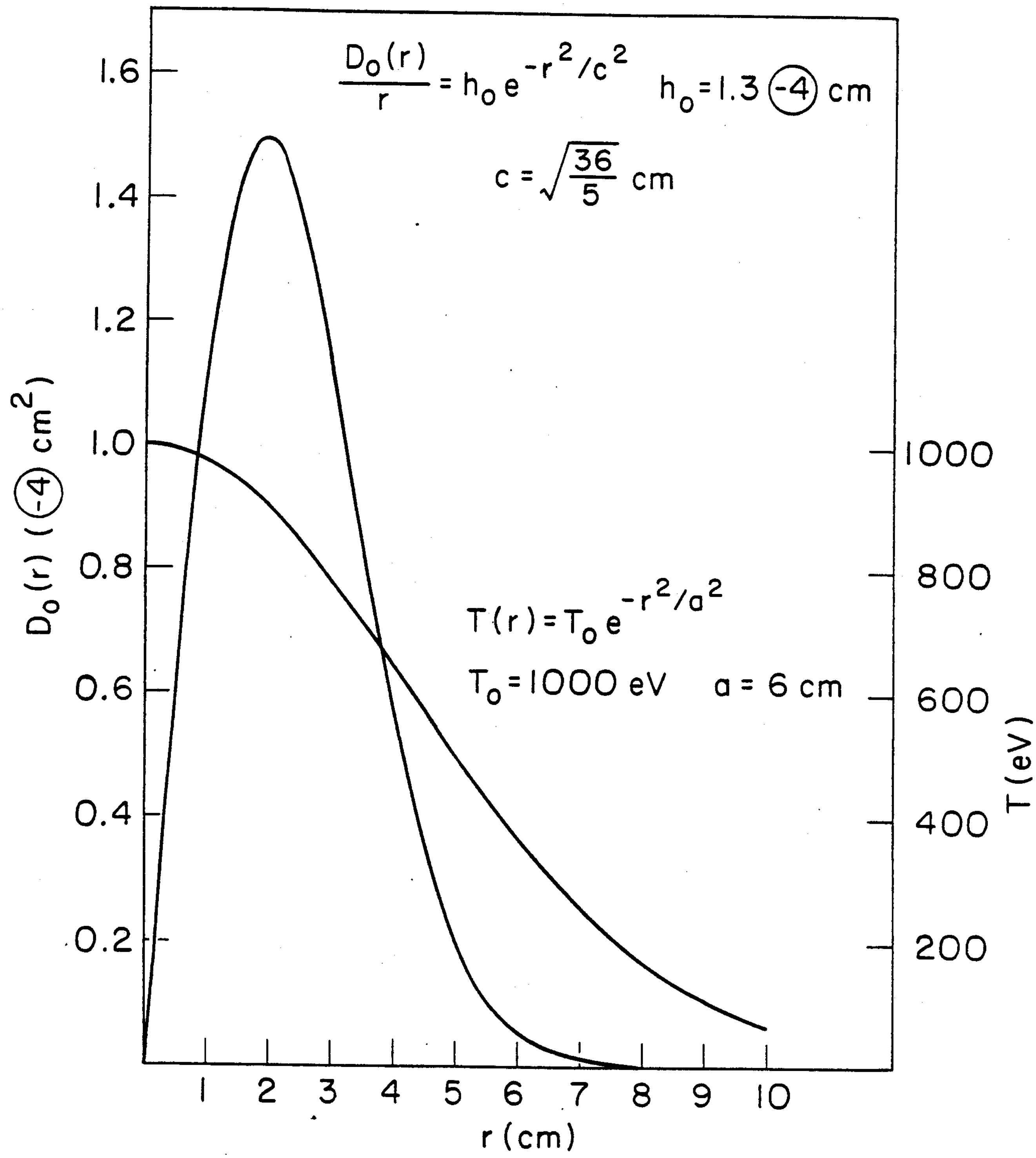

$\frac{D_0(r)}{r} = h_0 e^{-r^2/c^2}$
$h_0 = 1.3$ (-4) cm
$c = \sqrt{\frac{36}{5}}$ cm
$T(r) = T_0 e^{-r^2/a^2}$
$T_0 = 1000$ eV   a = 6 cm
1.6
1.4
1.2
1.0
0.8
0.6
0.4
0.2
$D_0(r)$ ((-4) cm^2)
1000
800
600
400
200
T (eV)
1
2
3
4
5
6
7
8
9
10
r (cm)

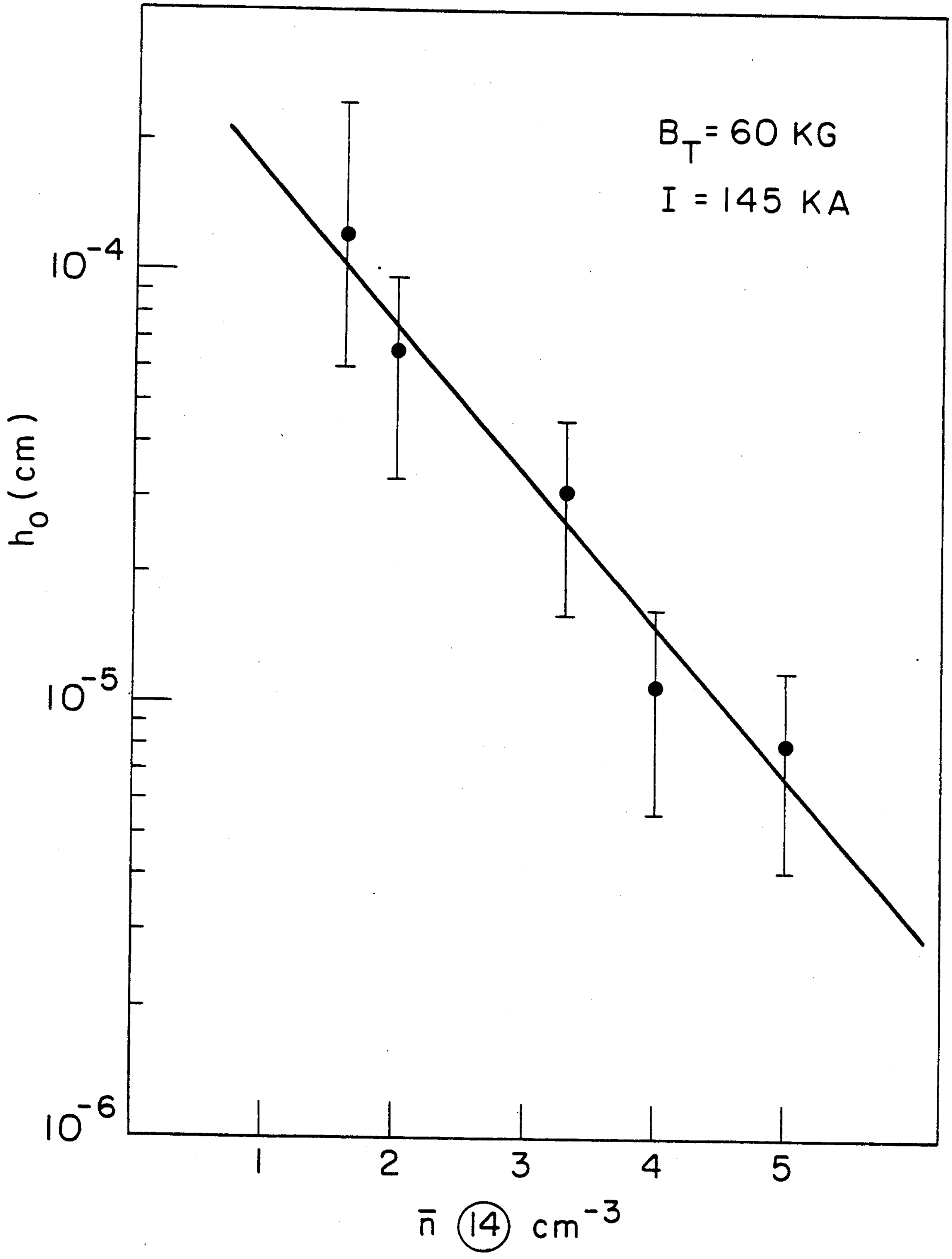
$B_T = 60$ KG
$I = 145$ KA
10^{-4}
10^{-5}
10^{-6}
h_o (cm)
1
2
3
4
5
$\bar{n}$ ⑭ cm^{-3}

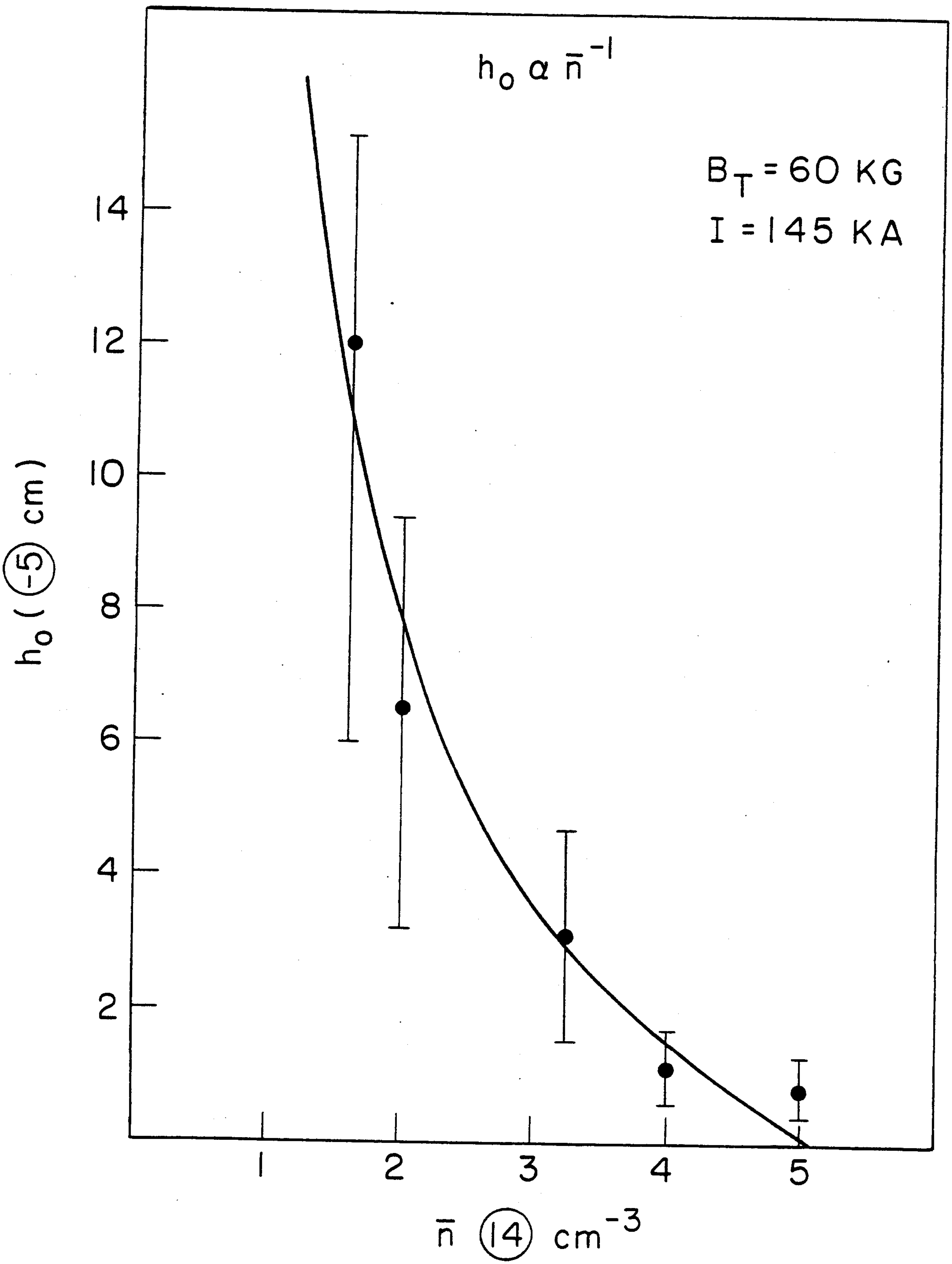
$h_o \alpha \bar{n}^{-1}$
$B_T = 60$ KG
I = 145 KA
h_o (⑤ cm)
14
12
10
8
6
4
2
1
2
3
4
5
$\bar{n}$ ⑭ cm^{-3}

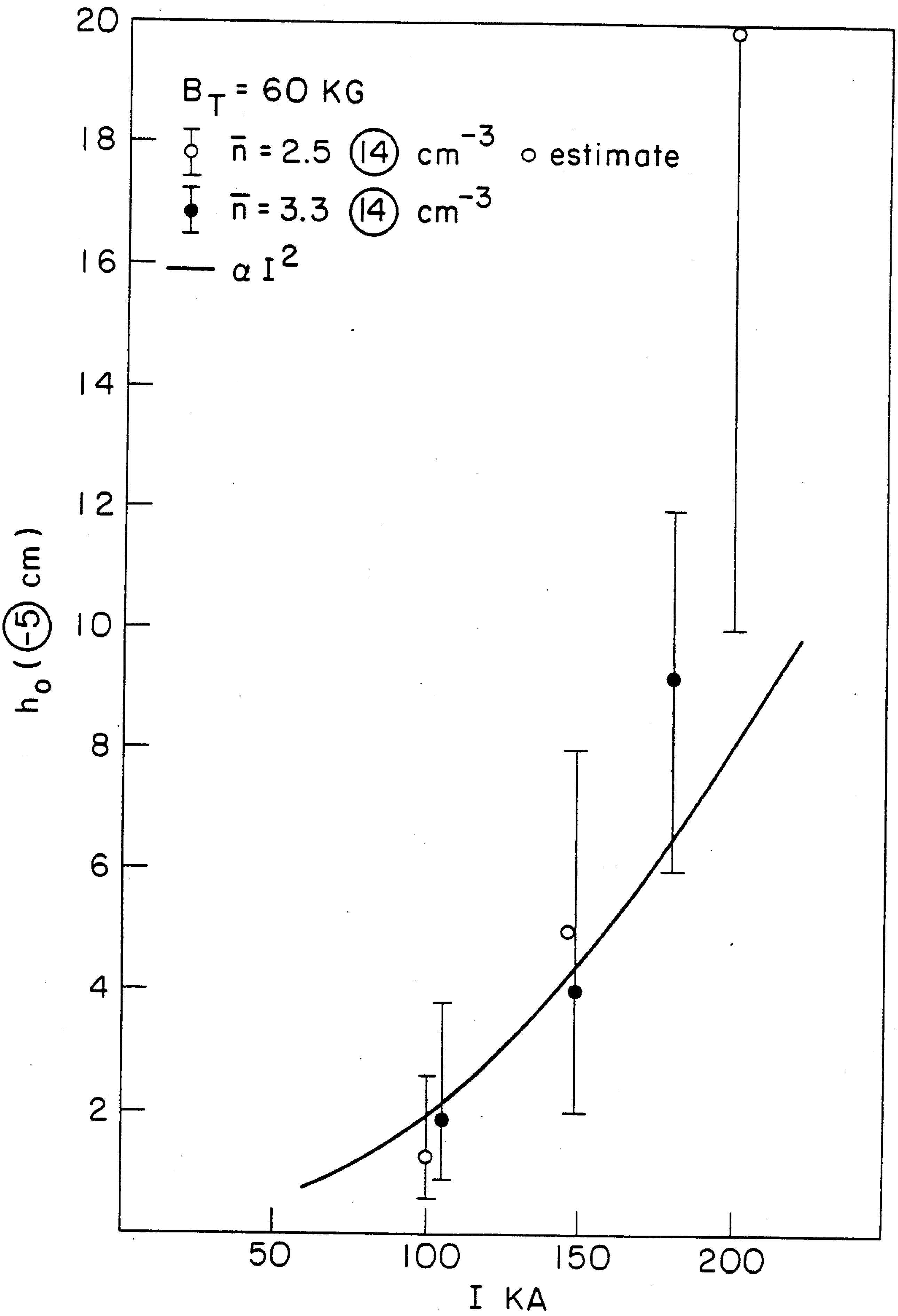
B_T = 60 KG
$\bar{n}$ = 2.5 ⑭ cm^{-3}
○ estimate
$\bar{n}$ = 3.3 ⑭ cm^{-3}
αI^2
20
18
16
14
12
10
8
6
4
2
h_o ((-5) cm)
50
100
150
200
I KA

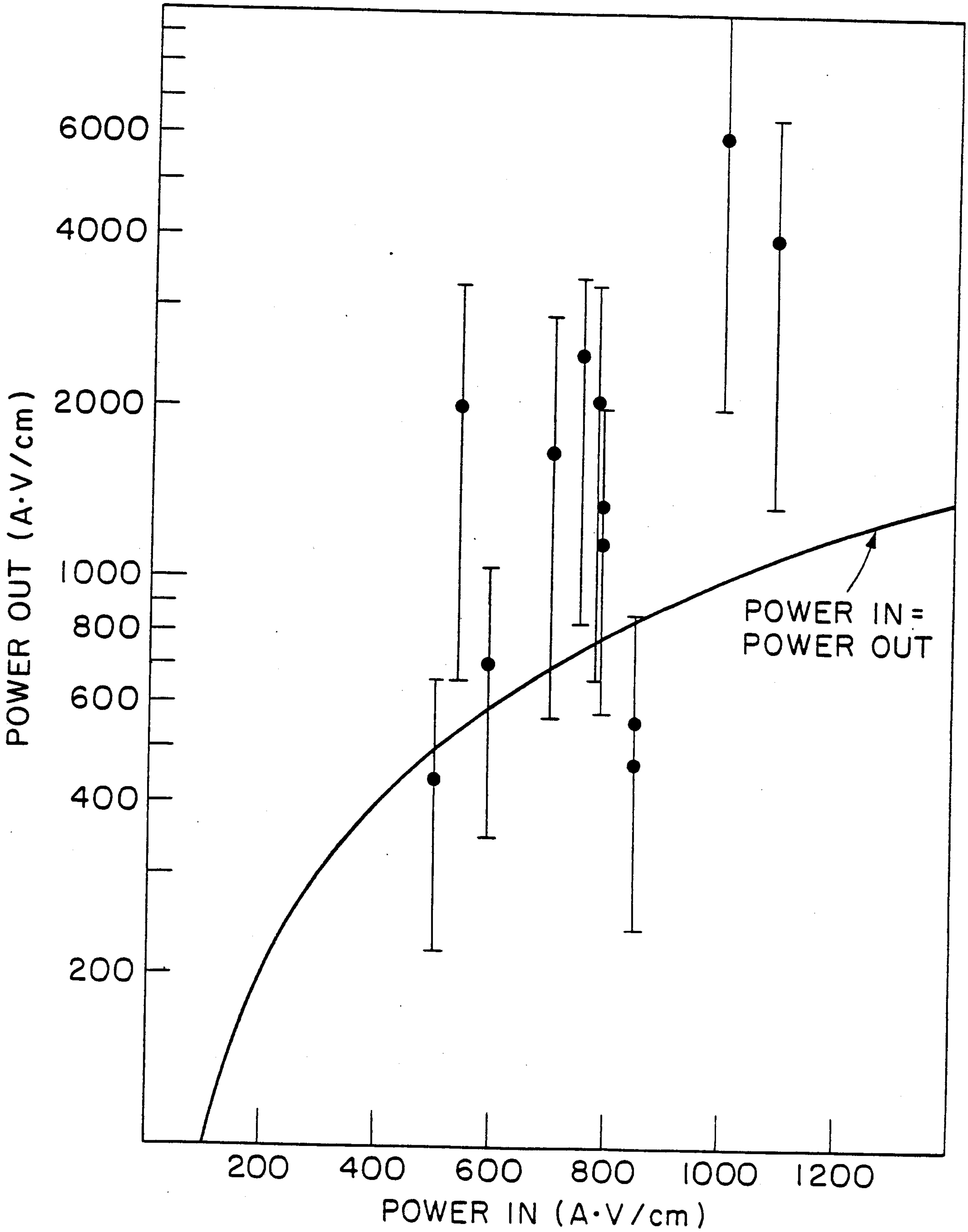

6000
4000
2000
1000
800
600
400
200
POWER OUT (A·V/cm)
200
400
600
800
1000
1200
POWER IN (A·V/cm)
POWER IN =
POWER OUT